Chapter 7

Bodies of Revolution

In this chapter we use the Method of Moments to solve surface integral equation problems involving bodies of revolution (BoRs), which includes objects such as spheres, ellipsoids, and finite cylinders. This is of practical interest, as objects like these are commonly used to benchmark computational electromagnetics techniques and codes, and to calibrate instruments that measure RCS in a static range. Many realistic objects, such as conic reentry vehicles (RVs), can also be modeled as bodies of revolution.

In Chapter 6, we solved the EFIE, MFIE, and nMFIE by formulating the common functional expressions (L, nL, K, and nK), and then assembled the MoM system matrix using those functions. In this chapter, we use the same methodology to treat BoRs of general shape and configuration. We will first discuss surface modeling and surface current expansion, and then derive the expressions required for each integral equation. We also discuss the treatment of junctions where three or more dielectric and/or conducting regions meet.

7.1 BoR Surface Description

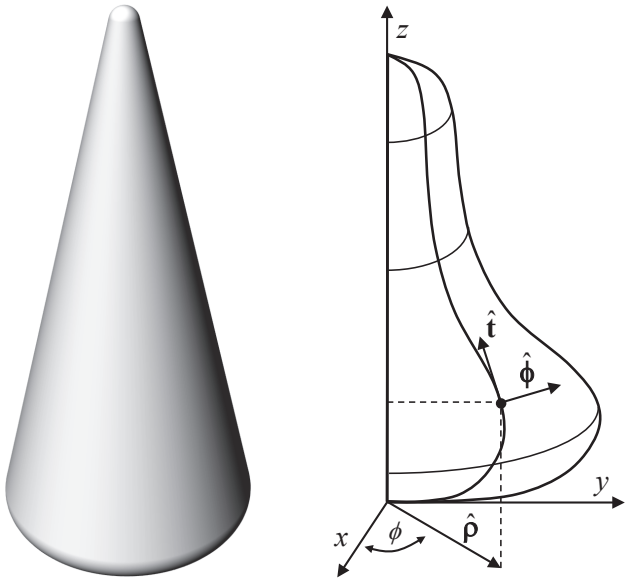
Consider a body of revolution such as the cone-sphere in Figure 7.1a. Such an object can be completely described by a bounding curve and an axis of symmetry, where rotating the bounding curve by 2π around the symmetry axis sweeps out the entire surface. We define a BoR in the cylindrical coordinate system shown in Figure 7.1b. In this system, the axis of symmetry is the $\hat{\mathbf{z}}$ axis, and any point $\mathbf{r}$ on the surface can be identified by its cylindrical components (ρ, ϕ, z) or by its corresponding Cartesian components, given by

$$\mathbf{r} = \rho\cos\phi\hat{\mathbf{x}} + \rho\sin\phi\hat{\mathbf{y}} + z\hat{\mathbf{z}}\,. \tag{7.1}$$

The distance r between any two points on the surface can be written as

$$r = |\mathbf{r} - \mathbf{r}'| = \sqrt{(\rho-\rho')^2 + (z-z')^2 + 2\rho\rho'[1-\cos(\phi-\phi')]}\,. \tag{7.2}$$

We next define the longitudinal vector $\hat{\mathbf{t}}(\mathbf{r})$, which along with the cylindrical vector $\hat{\boldsymbol{\phi}}(\mathbf{r})$, is everywhere tangent to the surface. Given the surface normal $\hat{\mathbf{n}}(\mathbf{r})$, they are



(a) Cone-Sphere (b) Local BoR Geometry

Figure 7.1: Body of Revolution (BoR)

related as

$$\hat{\mathbf{n}}(\mathbf{r}) = \hat{\boldsymbol{\phi}}(\mathbf{r}) \times \hat{\mathbf{t}}(\mathbf{r}) \; . \tag{7.3}$$

As $\hat{\mathbf{t}}(\mathbf{r})$ and $\hat{\boldsymbol{\phi}}(\mathbf{r})$ are everywhere normal to each other, they comprise an orthogonal basis set that we will use to expand the surface currents.

7.2 Expansion of Surface Currents

Due to the rotational symmetry, we will describe the surface currents **J** and **M** using $\hat{\mathbf{t}}$- and $\hat{\boldsymbol{\phi}}$-oriented basis functions that are local in the longitudinal dimension and a Fourier series in the azimuthal dimension [1]. In a region R_l with bounding surface S_l, the electric current is expanded using N basis functions of each type ($2N$ total basis functions), yielding [2]

$$\mathbf{J}_l(\mathbf{r}) = \sum_{\alpha=-\infty}^{\infty} \sum_{n=1}^{N} \Big[I_{\alpha n}^{J,t} \mathbf{f}_{\alpha n}^{t}(\mathbf{r}) - I_{\alpha n}^{J,\phi} \mathbf{f}_{\alpha n}^{\phi}(\mathbf{r}) \Big], \tag{7.4}$$

where $I_{\alpha n}^{J,t}$ and $I_{\alpha n}^{J,\phi}$ are the longitudinal and azimuthal expansion coefficients of basis function n for Fourier mode α. The functions $\mathbf{f}_{\alpha n}^{t,\phi}(\mathbf{r})$ are

$$\mathbf{f}_{\alpha n}^{t}(\mathbf{r}) = f_n(t) \; e^{j\alpha\phi} \; \hat{\mathbf{t}}(\mathbf{r}) \tag{7.5}$$

and

$$\mathbf{f}_{\alpha n}^{\phi}(\mathbf{r}) = f_n(t) \; e^{j\alpha\phi} \; \hat{\boldsymbol{\phi}}(\mathbf{r}) \; , \tag{7.6}$$

where for the one-dimensional function $f_n(t)$ we will use triangle functions (Section 2.3.2). For convenience, we will treat the integrations in the t dimension in a generic sense in the derivations that follow, and present a more detailed discussion in Section 7.7. Similarly, the magnetic current in R_l is

$$\mathbf{M}_l(\mathbf{r}) = \sum_{\alpha=-\infty}^{\infty} \sum_{n=1}^{N} \left[I_{\alpha n}^{M,t} \mathbf{g}_{\alpha n}^{t}(\mathbf{r}) - I_{\alpha n}^{M,\phi} \mathbf{g}_{\alpha n}^{\phi}(\mathbf{r}) \right] \tag{7.7}$$

where the functions $\mathbf{g}_{\alpha n}^{t,\phi}(\mathbf{r})$ are

$$\mathbf{g}_{\alpha n}^{t}(\mathbf{r}) = \eta_0 \; g_n(t) \; e^{j\alpha\phi} \; \hat{\mathbf{t}}(\mathbf{r}) \tag{7.8}$$

and

$$\mathbf{g}_{\alpha n}^{\phi}(\mathbf{r}) = \eta_0 \; g_n(t) \; e^{j\alpha\phi} \; \hat{\boldsymbol{\phi}}(\mathbf{r}) \; . \tag{7.9}$$

As it will simplify several expressions later, $f_n(t)$ and $g_n(t)$ are defined as

$$f_n(t) = g_n(t) = \frac{T_n(t)}{\rho(t)} \; , \tag{7.10}$$

where $T_n(t)$ is the triangle function. The minus sign on the second term in (7.4) and (7.7) was chosen as it will yield symmetries in several terms in the sections that follow.

7.3 EFIE

The EFIE (3.181) contains $\mathcal{L}$ and $\mathcal{K}$ operators, which were discretized and tested via the MoM in (3.188) and (3.189). To implement these on a BoR, we require expressions for the testing functions. Following the approach in [1], we will use the complex conjugate of the basis functions as the electric testing functions. Taking the conjugate of the $\hat{\mathbf{t}}$ and $\hat{\boldsymbol{\phi}}$ components from (7.5) and (7.6) yields

$$\mathbf{f}_{\beta m}^{t}(\mathbf{r}) = f_m(t) \; e^{-j\beta\phi} \; \hat{\mathbf{t}}(\mathbf{r}) \tag{7.11}$$

and

$$\mathbf{f}_{\beta m}^{\phi}(\mathbf{r}) = f_m(t) \; e^{-j\beta\phi} \; \hat{\boldsymbol{\phi}}(\mathbf{r}) \; . \tag{7.12}$$

7.3.1 $\mathcal{L}$ Operator

Substitution of the basis (7.5, 7.6) and testing (7.11, 7.12) functions into (3.188) yields a matrix of the form

$$Z^{EJ(l)} = \begin{bmatrix} \mathrm{L}(\mathbf{f}_{\beta}^{t}, \mathbf{f}_{\alpha}^{t}) & \mathrm{L}(\mathbf{f}_{\beta}^{t}, \mathbf{f}_{\alpha}^{\phi}) \\ \mathrm{L}(\mathbf{f}_{\beta}^{\phi}, \mathbf{f}_{\alpha}^{t}) & \mathrm{L}(\mathbf{f}_{\beta}^{\phi}, \mathbf{f}_{\alpha}^{\phi}) \end{bmatrix} = \begin{bmatrix} \mathrm{L}^{tt} & \mathrm{L}^{t\phi} \\ \mathrm{L}^{\phi t} & \mathrm{L}^{\phi\phi} \end{bmatrix} , \tag{7.13}$$

where in region R_l, the elements of each sub-matrix block are given by

$$\mathrm{L}^{**}_{mn} = j\omega\mu_l \int_{\mathbf{f}^{t,\phi}_{\beta m}} \int_{\mathbf{f}^{t,\phi}_{\alpha n}} \mathbf{f}^{t,\phi}_{\beta m}(\mathbf{r}) \cdot \pm\, \mathbf{f}^{t,\phi}_{\alpha n}(\mathbf{r}') \frac{e^{-jk_l r}}{4\pi r}\, d\mathbf{r}'\, d\mathbf{r}$$
$$-\frac{j}{\omega\epsilon_l} \int_{\mathbf{f}^{t,\phi}_{\beta m}} \int_{\mathbf{f}^{t,\phi}_{\alpha n}} \Big[\nabla \cdot \mathbf{f}^{t,\phi}_{\beta m}(\mathbf{r})\Big] \Big[\nabla' \cdot \pm\, \mathbf{f}^{t,\phi}_{\alpha n}(\mathbf{r}')\Big] \frac{e^{-jk_l r}}{4\pi r}\, d\mathbf{r}'\, d\mathbf{r}\,, \tag{7.14}$$

and we have used (3.207) to re-distribute the differential operators. The $\hat{\mathbf{t}}$- and $\hat{\boldsymbol{\phi}}$-oriented basis functions (7.14) have positive and negative signs, respectively, following the convention in (7.4).

7.3.1.1 L Matrix Elements

To compute the sub-matrix elements in (7.14) we must first determine the divergences of the basis and testing functions. These are

$$\nabla' \cdot \mathbf{f}^{t}_{\alpha n}(\mathbf{r}') = \frac{1}{\rho(t')} \frac{\partial}{\partial t'} \Big[\rho(t') f_n(t')\Big] e^{j\alpha\phi'} = \frac{1}{\rho(t')} T'_n(t') e^{j\alpha\phi'}\,, \tag{7.15}$$

$$\nabla \cdot \mathbf{f}^{t}_{\beta m}(\mathbf{r}) = \frac{1}{\rho(t)} \frac{\partial}{\partial t} \Big[\rho(t) f_m(t)\Big] e^{-j\beta\phi} = \frac{1}{\rho(t)} T'_m(t) e^{-j\beta\phi}\,, \tag{7.16}$$

$$\nabla' \cdot \mathbf{f}^{\phi}_{\alpha n}(\mathbf{r}') = \frac{f_n(t')}{\rho(t')} \frac{\partial}{\partial \phi'} e^{j\alpha\phi'} = \frac{j\alpha}{\rho(t')^2} T_n(t') e^{j\alpha\phi'}\,, \tag{7.17}$$

$$\nabla \cdot \mathbf{f}^{\phi}_{\beta m}(\mathbf{r}) = \frac{f_m(t)}{\rho(t)} \frac{\partial}{\partial \phi} e^{-j\beta\phi} = -\frac{j\beta}{\rho(t)^2} T_m(t) e^{-j\beta\phi}\,. \tag{7.18}$$

Using (7.15–7.18) and noting that the differential surface element in cylindrical coordinates is $ds = \rho d\phi dt$, the sub-matrix elements can be written as

$$\mathrm{L}^{tt}_{mn} = \int_{T_m} \int_{T_n} \int_0^{2\pi} \int_0^{2\pi} \Big[j\omega\mu_l T_m(t) T_n(t')\, \hat{\mathbf{t}}(\mathbf{r}) \cdot \hat{\mathbf{t}}(\mathbf{r}')$$
$$-\frac{j}{\omega\epsilon_l} T'_m(t) T'_n(t')\Big] e^{j(\alpha\phi' - \beta\phi)} \frac{e^{-jk_l r}}{4\pi r}\, d\phi'\, d\phi\, dt'\, dt\,, \tag{7.19}$$

$$\mathrm{L}^{t\phi}_{mn} = -\int_{T_m} \int_{T_n} \int_0^{2\pi} \int_0^{2\pi} \Big[j\omega\mu_l T_m(t) T_n(t')\, \hat{\mathbf{t}}(\mathbf{r}) \cdot \hat{\boldsymbol{\phi}}(\mathbf{r}')$$
$$+\frac{\alpha}{\omega\epsilon_l \rho(t')} T'_m(t) T_n(t')\Big] e^{j(\alpha\phi' - \beta\phi)} \frac{e^{-jk_l r}}{4\pi r}\, d\phi'\, d\phi\, dt'\, dt\,, \tag{7.20}$$

$$\mathrm{L}^{\phi t}_{mn} = \int_{T_m} \int_{T_n} \int_0^{2\pi} \int_0^{2\pi} \Big[j\omega\mu_l T_m(t) T_n(t')\, \hat{\boldsymbol{\phi}}(\mathbf{r}) \cdot \hat{\mathbf{t}}(\mathbf{r}')$$
$$-\frac{\beta}{\omega\epsilon_l \rho(t)} T_m(t) T'_n(t')\Big] e^{j(\alpha\phi' - \beta\phi)} \frac{e^{-jk_l r}}{4\pi r}\, d\phi'\, d\phi\, dt'\, dt\,, \tag{7.21}$$

$$\mathrm{L}^{\phi\phi}_{mn} = -\int_{T_m} \int_{T_n} \int_0^{2\pi} \int_0^{2\pi} \Big[j\omega\mu_l T_m(t) T_n(t')\, \hat{\boldsymbol{\phi}}(\mathbf{r}) \cdot \hat{\boldsymbol{\phi}}(\mathbf{r}')$$
$$-\frac{j\alpha\beta}{\omega\epsilon_l \rho(t)\rho(t')} T_m(t) T_n(t')\Big] e^{j(\alpha\phi' - \beta\phi)} \frac{e^{-jk_l r}}{4\pi r}\, d\phi'\, d\phi\, dt'\, dt\,. \tag{7.22}$$

We note that because integrals are periodic functions of ϕ' with period 2π, ϕ' can be replaced by $\phi' + \phi$ without altering their values [1]. Making this substitution allows us to write

$$\int_0^{2\pi} e^{j(\alpha\phi' - \beta\phi)}\, d\phi = e^{j\alpha\phi'} \int_0^{2\pi} e^{j(\alpha-\beta)\phi}\, d\phi\,, \tag{7.23}$$

and noting that

$$\int_0^{2\pi} e^{j(\alpha-\beta)\phi}\, d\phi = \begin{cases} 0 & \alpha \neq \beta \\ 2\pi & \alpha = \beta \end{cases}\,, \tag{7.24}$$

only those integrals where $\alpha = \beta$ will remain. Additionally, we observe that for a BoR,

$$\frac{e^{jkr(\rho,-\phi,z)}}{r(\rho,-\phi,z)} = \frac{e^{jkr(\rho,\phi,z)}}{r(\rho,\phi,z)} \qquad 0 \leq \phi \leq \pi\,. \tag{7.25}$$

Let us now define $\hat{\mathbf{t}}(\mathbf{r})$ such that

$$\hat{\mathbf{t}}(\mathbf{r}) = \sin\gamma\hat{\boldsymbol{\rho}} + \cos\gamma\hat{\mathbf{z}}\,, \tag{7.26}$$

which allows us to write the following dot products:

$$\hat{\mathbf{t}}(\mathbf{r}) \cdot \hat{\mathbf{t}}(\mathbf{r}') = \sin\gamma\sin\gamma'\cos(\phi' - \phi) + \cos\gamma\cos\gamma'\,, \tag{7.27}$$

$$\hat{\mathbf{t}}(\mathbf{r}) \cdot \hat{\boldsymbol{\phi}}(\mathbf{r}') = -\sin\gamma\sin(\phi' - \phi)\,, \tag{7.28}$$

$$\hat{\boldsymbol{\phi}}(\mathbf{r}) \cdot \hat{\mathbf{t}}(\mathbf{r}') = \sin\gamma'\sin(\phi' - \phi)\,, \tag{7.29}$$

$$\hat{\boldsymbol{\phi}}(\mathbf{r}) \cdot \hat{\boldsymbol{\phi}}(\mathbf{r}') = \cos(\phi' - \phi)\,. \tag{7.30}$$

Taking into account (7.27–7.30), and using the orthogonality relationships that exist between the trigonometric terms in the various integrands, the sub-matrix elements are:

$$\begin{aligned} \mathrm{L}_{mn}^{tt} = &\int_{T_m}\int_{T_n} \Big[j\omega\mu_l T_m(t)T_n(t')\big(\sin\gamma\sin\gamma' G_2 + \cos\gamma\cos\gamma' G_1\big) \\ &-\frac{j}{\omega\epsilon_l} T_m'(t)T_n'(t')G_1 \Big]\, dt'\, dt\,, \end{aligned} \tag{7.31}$$

$$\mathrm{L}_{mn}^{t\phi} = -\int_{T_m}\int_{T_n} \Big[\omega\mu_l T_m(t)T_n(t')\sin\gamma G_3 + \frac{\alpha}{\omega\epsilon_l\rho(t')} T_m'(t)T_n(t')G_1 \Big]\, dt'\, dt\,, \tag{7.32}$$

$$\mathrm{L}_{mn}^{\phi t} = -\int_{T_m}\int_{T_n} \Big[\omega\mu_l T_m(t)T_n(t')\sin\gamma' G_3 + \frac{\alpha}{\omega\epsilon_l\rho(t)} T_m(t)T_n'(t')G_1 \Big]\, dt'\, dt\,, \tag{7.33}$$

$$\mathrm{L}_{mn}^{\phi\phi} = -\int_{T_m}\int_{T_n} \Big[j\omega\mu_l T_m(t)T_n(t')G_2 - \frac{j\alpha^2}{\omega\epsilon_l\rho(t)\rho(t')} T_m(t)T_n(t')G_1 \Big]\, dt'\, dt\,. \tag{7.34}$$

where the integrals G_1, G_2 and G_3 are

$$G_1 = \int_0^{\pi} \cos(\alpha\phi')\frac{e^{-jk_l r}}{r} d\phi'\,, \tag{7.35}$$

$$G_2 = \int_0^{\pi} \cos(\phi')\cos(\alpha\phi')\frac{e^{-jk_l r}}{r} d\phi'\,, \tag{7.36}$$

$$G_3 = \int_0^{\pi} \sin(\phi')\sin(\alpha\phi')\frac{e^{-jk_l r}}{r} d\phi'\,. \tag{7.37}$$

These integrals are evaluated by a one-dimensional Gaussian quadrature. When $\mathbf{r} \neq \mathbf{r}'$, r can be obtained via

$$r = |\mathbf{r} - \mathbf{r}'| = \sqrt{(\rho - \rho')^2 + (z - z')^2 + 2\rho\rho'[1 - \cos(\phi')]}\,. \tag{7.38}$$

When $\mathbf{r} = \mathbf{r}'$, a modification of (7.38) for the above is needed, which is discussed in Section 7.7.

Inspecting the L sub-matrix elements, we find that the relationship between positive and negative modes is

$$\begin{bmatrix} \mathrm{L}^{tt} & \mathrm{L}^{t\phi} \\ \mathrm{L}^{\phi t} & \mathrm{L}^{\phi\phi} \end{bmatrix}_{-\alpha} = \begin{bmatrix} \mathrm{L}^{tt} & -\mathrm{L}^{t\phi} \\ -\mathrm{L}^{\phi t} & \mathrm{L}^{\phi\phi} \end{bmatrix}_{\alpha}. \tag{7.39}$$

These properties survive inversion.

7.3.2 $\mathcal{K}$ Operator

Substitution of the magnetic basis and electric testing functions into (3.189) yields a matrix of the form

$$Z^{EM(l)} = \begin{bmatrix} \mathrm{K}(\mathbf{f}^t_\beta, \mathbf{g}^t_\alpha) & \mathrm{K}(\mathbf{f}^t_\beta, \mathbf{g}^\phi_\alpha) \\ \mathrm{K}(\mathbf{f}^\phi_\beta, \mathbf{g}^t_\alpha) & \mathrm{K}(\mathbf{f}^\phi_\beta, \mathbf{g}^\phi_\alpha) \end{bmatrix} = \begin{bmatrix} \mathrm{K}^{tt} & \mathrm{K}^{t\phi} \\ \mathrm{K}^{\phi t} & \mathrm{K}^{\phi\phi} \end{bmatrix}, \tag{7.40}$$

where in Region R_l, the elements of each sub-matrix block are given by

$$\begin{aligned} \mathrm{K}^{**}_{mn} =& \frac{1}{2} \int_{\mathbf{f}^{t,\phi}_{\beta m}, \mathbf{g}^{t,\phi}_{\alpha n}} \mathbf{f}^{t,\phi}_{\beta m}(\mathbf{r}) \cdot \left[\hat{\mathbf{n}}_l(\mathbf{r}) \times \pm\, \mathbf{g}^{t,\phi}_{\alpha n}(\mathbf{r})\right] d\mathbf{r} \\ & - \int_{\mathbf{f}^{t,\phi}_{\beta m}} \mathbf{f}^{t,\phi}_{\beta m}(\mathbf{r}) \cdot \int_{\mathbf{g}^{t,\phi}_{\alpha n}} \left[(\mathbf{r} - \mathbf{r}') \times \pm\, \mathbf{g}^{t,\phi}_{\alpha n}(\mathbf{r}')\right] \frac{1 + jk_l r}{4\pi r^3} e^{-jk_l r}\, d\mathbf{r}' d\mathbf{r}\,. \end{aligned} \tag{7.41}$$

7.3.2.1 K Matrix Elements

To evaluate the sub-matrix elements in (7.41), let us first make the following definitions

$$\mathbf{r} = \rho\hat{\boldsymbol{\rho}} + z\hat{\mathbf{z}}\,, \tag{7.42}$$

$$\mathbf{r}' = \rho'\cos(\phi' - \phi)\hat{\boldsymbol{\rho}} + \rho'\sin(\phi' - \phi)\hat{\boldsymbol{\phi}} + z'\hat{\mathbf{z}}\,, \tag{7.43}$$

$$\hat{\mathbf{t}}(\mathbf{r}') = \sin\gamma'\Big[\cos(\phi' - \phi)\hat{\boldsymbol{\rho}} + \sin(\phi' - \phi)\hat{\boldsymbol{\phi}}\Big] + \cos\gamma'\hat{\mathbf{z}}\,, \tag{7.44}$$

$$\hat{\boldsymbol{\phi}}(\mathbf{r}') = -\sin(\phi' - \phi)\hat{\boldsymbol{\rho}} + \cos(\phi' - \phi)\hat{\boldsymbol{\phi}}\,, \tag{7.45}$$

and then compute the following cross products

$$\begin{aligned} (\mathbf{r} - \mathbf{r}') \times \hat{\mathbf{t}}(\mathbf{r}') =& \sin(\phi' - \phi)\Big[(z' - z)\sin\gamma' - \rho'\cos\gamma'\Big]\hat{\boldsymbol{\rho}} \\ & - \Big[\big(\rho - \rho'\cos(\phi' - \phi)\big)\cos\gamma' + (z' - z)\sin\gamma'\cos(\phi' - \phi)\Big]\hat{\boldsymbol{\phi}} \\ & + \rho\sin\gamma'\sin(\phi' - \phi)\hat{\mathbf{z}}\,, \end{aligned} \tag{7.46}$$

and

$$(\mathbf{r}-\mathbf{r}')\times\hat{\boldsymbol{\phi}}(\mathbf{r}') = (z'-z)\cos(\phi'-\phi)\hat{\boldsymbol{\rho}} + (z'-z)\sin(\phi'-\phi)\hat{\boldsymbol{\phi}} + \Big[\rho\cos(\phi'-\phi)-\rho'\Big]\hat{\mathbf{z}}\,. \tag{7.47}$$

These definitions then allow us to write

$$\hat{\mathbf{t}}(\mathbf{r})\cdot\Big[(\mathbf{r}-\mathbf{r}')\times\hat{\mathbf{t}}(\mathbf{r}')\Big] = \Big[(z'-z)\sin\gamma\sin\gamma' - \rho'\cos\gamma'\sin\gamma + \rho\cos\gamma\sin\gamma'\Big]\sin(\phi'-\phi)\,, \tag{7.48}$$

$$\hat{\mathbf{t}}(\mathbf{r})\cdot\Big[(\mathbf{r}-\mathbf{r}')\times\hat{\boldsymbol{\phi}}(\mathbf{r}')\Big] = \Big[(z'-z)\sin\gamma\cos(\phi'-\phi) + \big[\rho\cos(\phi'-\phi)-\rho'\big]\cos\gamma\Big], \tag{7.49}$$

$$\hat{\boldsymbol{\phi}}(\mathbf{r})\cdot\Big[(\mathbf{r}-\mathbf{r}')\times\hat{\mathbf{t}}(\mathbf{r}')\Big] = -\Big[(z'-z)\sin\gamma'\cos(\phi'-\phi) + \big[\rho-\rho'\cos(\phi'-\phi)\big]\cos\gamma'\Big], \tag{7.50}$$

$$\hat{\boldsymbol{\phi}}(\mathbf{r})\cdot\Big[(\mathbf{r}-\mathbf{r}')\times\hat{\boldsymbol{\phi}}(\mathbf{r}')\Big] = (z'-z)\sin(\phi'-\phi)\,. \tag{7.51}$$

Using (7.48–7.51) as well as the periodic properties of the integrands outlined in Section 7.3.1.1, the system matrix can be re-written as

$$\begin{bmatrix} \mathrm{K}^{tt} & \mathrm{K}^{t\phi}+\tilde{\mathrm{K}}^{t\phi} \\ \mathrm{K}^{\phi t}+\tilde{\mathrm{K}}^{\phi t} & \mathrm{K}^{\phi\phi} \end{bmatrix}. \tag{7.52}$$

The sub-matrix elements for mode α are

$$\mathrm{K}^{tt}_{mn} = j\eta_0\int_{T_m}\int_{T_n} T_m(t)\,T_n(t')\,\Big(\big[z(t)-z(t')\big]\sin\gamma(t)\sin\gamma(t') + \sin\gamma(t)\cos\gamma(t')\rho(t') - \sin\gamma(t')\cos\gamma(t)\rho(t)\Big)G_6\;dt'\;dt\,, \tag{7.53}$$

$$\mathrm{K}^{t\phi}_{mn} = -\eta_0\int_{T_m}\int_{T_n} T_m(t)\,T_n(t')\cdot\Big(\big[z(t)-z(t')\big]\sin\gamma(t)G_5 + \cos\gamma(t)\big[\rho(t')G_4-\rho(t)G_5\big]\Big)\;dt'\;dt\,, \tag{7.54}$$

$$\mathrm{K}^{\phi t}_{mn} = -\eta_0\int_{T_m}\int_{T_n} T_m(t)\,T_n(t')\cdot\Big(\big[z(t)-z(t')\big]\sin\gamma(t')G_5 + \cos\gamma(t')\big[\rho(t')G_5-\rho(t)G_4\big]\Big)\;dt'\;dt\,, \tag{7.55}$$

$$\mathrm{K}^{\phi\phi}_{mn} = -j\eta_0\int_{T_m}\int_{T_n} T_m(t)\,T_n(t')\,\big[z(t)-z(t')\big]G_6\;dt'\;dt\,, \tag{7.56}$$

where these expressions apply to non-overlapping segments. For overlapping segments, the principal-value contribution is treated separately, giving

$$\tilde{\mathrm{K}}^{t\phi}_{mn} = \tilde{\mathrm{K}}^{\phi t}_{mn} = \tilde{\mathrm{K}}_{mn} = -\pi\eta_0\int_{T_m,T_n}\frac{T_m(t)T_n(t)}{\rho(t)}\;dt\,. \tag{7.57}$$

The integrals G_4, G_5, and G_6 are

$$G_4 = \int_0^\pi \cos(\alpha\phi') \frac{1 + jk_l r}{r^3} e^{-jk_l r} d\phi' \,, \tag{7.58}$$

$$G_5 = \int_0^\pi \cos(\phi') \cos(\alpha\phi') \frac{1 + jk_l r}{r^3} e^{-jk_l r} d\phi' \,, \tag{7.59}$$

$$G_6 = \int_0^\pi \sin(\phi') \sin(\alpha\phi') \frac{1 + jk_l r}{r^3} e^{-jk_l r} d\phi' \,, \tag{7.60}$$

where r was defined in (7.38).

Inspecting the K sub-matrix elements, we find that the relationship between positive and negative modes is

$$\begin{bmatrix} \mathrm{K}^{tt} & \mathrm{K}^{t\phi} \\ \mathrm{K}^{\phi t} & \mathrm{K}^{\phi\phi} \end{bmatrix}_{-\alpha} = \begin{bmatrix} -\mathrm{K}^{tt} & \mathrm{K}^{t\phi} \\ \mathrm{K}^{\phi t} & -\mathrm{K}^{\phi\phi} \end{bmatrix}_{\alpha} . \tag{7.61}$$

These properties survive inversion.

7.3.3 Excitation

Right-hand side vector elements for the EFIE can be obtained by substituting the testing functions $\mathbf{f}_{\alpha m}^{t,\phi}(\mathbf{r})$ into (3.194). This yields a column vector of the form

$$V^{E(l)} = \begin{bmatrix} V^{E(l),t} \\ V^{E(l),\phi} \end{bmatrix} . \tag{7.62}$$

The individual elements are given by

$$V_m^{E(l),(t,\phi)} = \int_{T_m} \int_0^{2\pi} \mathbf{f}_{\alpha m}^{t,\phi}(\mathbf{r}) \cdot \mathbf{E}^i(\mathbf{r}) \, \rho \, d\phi \, dt \,, \tag{7.63}$$

where $\mathbf{E}^i(\mathbf{r})$ is the impressed electric field. In general, the above integral must be evaluated numerically, however for plane waves it can be evaluated in the ϕ dimension analytically.

7.3.3.1 Plane Wave Excitation

An incident plane wave in the free space region R_0 has a phase component at a point $\mathbf{r}$ given by

$$e^{jk_0 \hat{\mathbf{r}}^i \cdot \mathbf{r}} = e^{jk_0 z \cos\theta^i} e^{jk_0 \sin\theta^i (x\cos\phi^i + y \sin\phi^i)} \,, \tag{7.64}$$

where (θ^i, ϕ^i) are the incident spherical angles, and $\hat{\mathbf{r}}^i$ the direction of incidence. In cylindrical coordinates, (7.64) can be written as

$$e^{jk_0 z \cos\theta^i} e^{jk_0 \sin\theta^i (x\cos\phi^i + y \sin\phi^i)} = e^{jk_0 z \cos\theta^i} e^{jk_0 \sin\theta^i \rho \cos(\phi - \phi^i)} \,. \tag{7.65}$$

To obtain a complete scattering matrix, we must consider $\hat{\boldsymbol{\theta}}^i$- and $\hat{\boldsymbol{\phi}}^i$-polarized incident waves, so we will treat each polarization separately. Using the fact that

$$\hat{\boldsymbol{\theta}}^i = \cos\theta^i \cos\phi^i \hat{\mathbf{x}} + \cos\theta^i \sin\phi^i \hat{\mathbf{y}} - \sin\theta^i \hat{\mathbf{z}} \,, \tag{7.66}$$

and

$$\hat{\boldsymbol{\phi}}^{\,i} = -\sin\phi^i\hat{\mathbf{x}} + \cos\phi^i\hat{\mathbf{y}}\,, \tag{7.67}$$

we take the dot products with the $\hat{\mathbf{t}}$ and $\hat{\boldsymbol{\phi}}$ component vectors to yield

$$\hat{\mathbf{t}}\cdot\hat{\boldsymbol{\theta}}^{\,i} = \cos\theta^i\sin\gamma\cos(\phi-\phi^i) - \sin\theta^i\cos\gamma\,, \tag{7.68}$$

$$\hat{\boldsymbol{\phi}}\cdot\hat{\boldsymbol{\theta}}^{\,i} = -\cos\theta^i\sin(\phi-\phi^i)\,, \tag{7.69}$$

$$\hat{\mathbf{t}}\cdot\hat{\boldsymbol{\phi}}^{\,i} = \sin\gamma\sin(\phi-\phi^i)\,, \tag{7.70}$$

$$\hat{\boldsymbol{\phi}}\cdot\hat{\boldsymbol{\phi}}^{\,i} = \cos(\phi-\phi^i)\,. \tag{7.71}$$

Testing the $\hat{\boldsymbol{\theta}}^{\,i}$-polarized electric field with the $\hat{\mathbf{t}}$ and $\hat{\boldsymbol{\phi}}$-oriented electric testing functions yields a right-hand side vector of the form

$$V^{E,\theta^i} = \begin{bmatrix} V^{E,t\theta^i} \\ V^{E,\phi\theta^i} \end{bmatrix}, \tag{7.72}$$

with elements given by

$$V_m^{E,t\theta^i} = \int_{T_m} T_m(t)e^{jk_0z(t)\cos\theta^i}\int_0^{2\pi}\Big[\cos\theta^i\sin\gamma(t)\cos\phi - \sin\theta^i\cos\gamma(t)\Big]\cdot e^{jk_0\sin\theta^i\rho(t)\cos\phi - j\alpha\phi}\,d\phi\,dt \tag{7.73}$$

and

$$V_m^{E,\phi\theta^i} = -\int_{T_m} T_m(t)e^{jk_0z(t)\cos\theta^i}\int_0^{2\pi}\cos\theta^i\sin\phi\cdot e^{jk_0\sin\theta^i\rho(t)\cos\phi - j\alpha\phi}\,d\phi\,dt\,. \tag{7.74}$$

Similarly, testing the $\hat{\boldsymbol{\phi}}^{\,i}$-polarized electric field yields a right-hand side vector of the form

$$V^{E,\phi^i} = \begin{bmatrix} V^{E,t\phi^i} \\ V^{E,\phi\phi^i} \end{bmatrix}, \tag{7.75}$$

with elements given by

$$V_m^{E,t\phi^i} = \int_{T_m} T_m(t)e^{jk_0z(t)\cos\theta^i}\int_0^{2\pi}\sin\gamma(t)\sin\phi\; e^{jk_0\sin\theta^i\rho(t)\cos\phi - j\alpha\phi}\,d\phi\,dt \tag{7.76}$$

and

$$V_m^{E,\phi\phi^i} = \int_{T_m} T_m(t)e^{jk_0z(t)\cos\theta^i}\int_0^{2\pi}\cos\phi\; e^{jk_0\sin\theta^i\rho(t)\cos\phi - j\alpha\phi}\,d\phi\,dt\,. \tag{7.77}$$

Due to the rotational symmetry, we have set ϕ^i to zero for simplicity. If we need to solve bistatic scattering problems, we can simply replace ϕ^s by $\phi^s - \phi^i$ when computing the scattered field in Section 7.5.2.1.

Let us now consider the innermost integral of $V_m^{E,t\theta^i}$ in (7.73), which is

$$I = \cos\theta^i \sin\gamma(t) \int_0^{2\pi} \cos\phi e^{jk_0 \sin\theta^i \rho(t) \cos\phi - j\alpha\phi}\, d\phi$$
$$- \sin\theta^i \cos\gamma(t) \int_0^{2\pi} e^{jk_0 \sin\theta^i \rho(t) \cos\phi - j\alpha\phi}\, d\phi\,. \tag{7.78}$$

Using the identity [3]

$$2\pi j^\alpha J_\alpha(z) = \int_0^{2\pi} e^{jz\cos\phi} \cos(\alpha\phi)\, d\phi\,, \tag{7.79}$$

the second integral in (7.78) is

$$\int_0^{2\pi} e^{jk_0 \sin\theta^i \rho(t) \cos\phi - j\alpha\phi}\, d\phi = 2\pi j^\alpha J_\alpha(x)\,, \tag{7.80}$$

where $x = k_0 \sin\theta^i \rho(t)$. We can then write (7.78) as

$$I = \cos\theta^i \sin\gamma(t) \int_0^{2\pi} \cos\phi e^{jk_0 \sin\theta^i \rho(t) \cos\phi - j\alpha\phi}\, d\phi$$
$$-2\pi j^\alpha J_\alpha(x) \sin\theta^i \cos\gamma(t)\,. \tag{7.81}$$

To evaluate the first integral in (7.78), we substitute $\cos\phi = e^{j\phi} - j\sin\phi$ to yield

$$\int_0^{2\pi} \cos\phi e^{jk_0 \sin\theta^i \rho(t) \cos\phi - j\alpha\phi}\, d\phi = \int_0^{2\pi} (e^{j\phi} - j\sin\phi) e^{jk_0 \sin\theta^i \rho(t) \cos\phi - j\alpha\phi}\, d\phi\,. \tag{7.82}$$

The first term is evaluated as before, yielding

$$2\pi j^{\alpha-1} J_{\alpha-1}(x) - j \int_0^{2\pi} \sin\phi e^{jk_0 \sin\theta^i \rho(t) \cos\phi - j\alpha\phi}\, d\phi\,, \tag{7.83}$$

and the second term can be integrated by parts, yielding

$$2\pi j^{\alpha-1} J_{\alpha-1}(x) + j\left[\frac{2\pi\alpha}{x} j^\alpha J_\alpha(x)\right]. \tag{7.84}$$

Using the recurrence relationship

$$\frac{2\alpha}{x} J_\alpha(x) = J_{\alpha+1}(x) + J_{\alpha-1}(x)\,, \tag{7.85}$$

we can write (7.84) as

$$\pi j^\alpha j\Big[J_{\alpha+1}(x) - J_{\alpha-1}(x)\Big]\,, \tag{7.86}$$

and $V_m^{E,t\theta^i}$ finally becomes

$$V_m^{E,t\theta^i} = \pi j^\alpha \int_{T_m} T_m(t) e^{jk_0 z(t)\cos\theta^i} \Big[j\cos\theta^i \sin\gamma(t)\big[J_{\alpha+1}(x) - J_{\alpha-1}(x)\big]$$
$$-2\sin\theta^i \cos\gamma(t) J_\alpha(x)\Big]\, dt\,. \tag{7.87}$$

The other elements are obtained similarly, yielding

$$V_m^{E,\phi\theta^i} = \pi j^\alpha \int_{T_m} T_m(t) e^{jk_0 z(t)\cos\theta^i} \cos\theta^i \Big[J_{\alpha+1}(x) + J_{\alpha-1}(x) \Big]\, dt\,, \tag{7.88}$$

$$V_m^{E,t\phi^i} = -\pi j^\alpha \int_{T_m} T_m(t) e^{jk_0 z(t)\cos\theta^i} \sin\gamma(t) \Big[J_{\alpha+1}(x) + J_{\alpha-1}(x) \Big]\, dt\,, \tag{7.89}$$

and

$$V_m^{E,\phi\phi^i} = \pi j^{\alpha+1} \int_{T_m} T_m(t) e^{jk_0 z(t)\cos\theta^i} \Big[J_{\alpha+1}(x) - J_{\alpha-1}(x) \Big]\, dt\,. \tag{7.90}$$

Inspecting (7.87–7.90), we find that the relationship between positive and negative modes is

$$\begin{bmatrix} V^{E,t\theta^i} \\ V^{E,\phi\theta^i} \end{bmatrix}_{-\alpha} = \begin{bmatrix} V^{E,t\theta^i} \\ -V^{E,\phi\theta^i} \end{bmatrix}_{\alpha} \tag{7.91}$$

and

$$\begin{bmatrix} V^{E,t\phi^i} \\ V^{E,\phi\phi^i} \end{bmatrix}_{-\alpha} = \begin{bmatrix} -V^{E,t\phi^i} \\ V^{E,\phi\phi^i} \end{bmatrix}_{\alpha}. \tag{7.92}$$

7.4 MFIE

The MFIE (3.182) also has $\mathcal{K}$ and $\mathcal{L}$ operators, which were discretized and tested via the MoM in (3.190) and (3.191). For the testing functions, we use the complex conjugates of the magnetic basis functions (7.8) and (7.9). Substitution of the electric basis and magnetic testing functions into (3.190) yields in region R_l a matrix of the form

$$Z_{mn}^{HJ(l)} = -\begin{bmatrix} \mathrm{K}(\mathbf{g}_\beta^t, \mathbf{f}_\alpha^t) & \mathrm{K}(\mathbf{g}_\beta^t, \mathbf{f}_\alpha^\phi) \\ \mathrm{K}(\mathbf{g}_\beta^\phi, \mathbf{f}_\alpha^t) & \mathrm{K}(\mathbf{g}_\beta^\phi, \mathbf{f}_\alpha^\phi) \end{bmatrix} = -\begin{bmatrix} \mathrm{K}^{tt} & \mathrm{K}^{t\phi} \\ \mathrm{K}^{\phi t} & \mathrm{K}^{\phi\phi} \end{bmatrix}, \tag{7.93}$$

and substitution of the magnetic basis and testing functions into (3.191) yields

$$Z_{mn}^{HM(l)} = \frac{\epsilon_l}{\mu_l} \begin{bmatrix} \mathrm{L}(\mathbf{g}_\beta^t, \mathbf{g}_\alpha^t) & \mathrm{L}(\mathbf{g}_\beta^t, \mathbf{g}_\alpha^\phi) \\ \mathrm{L}(\mathbf{g}_\beta^\phi, \mathbf{g}_\alpha^t) & \mathrm{L}(\mathbf{g}_\beta^\phi, \mathbf{g}_\alpha^\phi) \end{bmatrix} = \eta_0^2 \frac{\epsilon_l}{\mu_l} \begin{bmatrix} \mathrm{L}^{tt} & \mathrm{L}^{t\phi} \\ \mathrm{L}^{\phi t} & \mathrm{L}^{\phi\phi} \end{bmatrix}, \tag{7.94}$$

where the expressions for the L and K sub-matrix elements were derived previously in Sections 7.3.1.1 and 7.3.2.1, respectively.

7.4.1 Excitation

Right-hand side vector elements for the MFIE can be obtained by substituting the testing functions $\mathbf{g}_{\alpha m}^{t,\phi}(\mathbf{r})$ into (3.195). This yields a column vector of length $2N$ of the form

$$V^{H(l)} = \begin{bmatrix} V^{H(l),t} \\ V^{H(l),\phi} \end{bmatrix}. \tag{7.95}$$

The individual elements are given by

$$V_m^{H(l),(t,\phi)} = \int_{T_m} \int_0^{2\pi} \mathbf{g}_{\alpha m}^{t,\phi}(\mathbf{r}) \cdot \mathbf{H}^i(\mathbf{r}) \; \rho \; d\phi \; dt \; , \tag{7.96}$$

where $\mathbf{H}^i(\mathbf{r})$ is the impressed magnetic field. As with the EFIE, this can be evaluated analytically in the ϕ dimension for incident plane waves.

7.4.1.1 Plane Wave Excitation

Given planar, $\hat{\boldsymbol{\theta}}^i$- and $\hat{\boldsymbol{\phi}}^i$-polarized incident electric fields, the corresponding magnetic fields are $-\hat{\boldsymbol{\phi}}^i$- and $\hat{\boldsymbol{\theta}}^i$-polarized, respectively. Thus, we can re-use the components of $V^{E(l)}$, yielding MFIE right-hand side vectors given by

$$V^{H,\theta^i} = \begin{bmatrix} V^{H,t\theta^i} \\ V^{H,\phi\theta^i} \end{bmatrix} = \begin{bmatrix} -V^{E,t\phi^i} \\ -V^{E,\phi\phi^i} \end{bmatrix} , \tag{7.97}$$

and

$$V^{H,\phi^i} = \begin{bmatrix} V^{H,t\phi^i} \\ V^{H,\phi\phi^i} \end{bmatrix} = \begin{bmatrix} V^{E,t\theta^i} \\ V^{E,\phi\theta^i} \end{bmatrix} . \tag{7.98}$$

7.5 Solution

Assembling the sub-matrix blocks for the EFIE and MFIE, the system matrix (3.187) for a general BoR has the form

$$\begin{bmatrix} Z^{EJ,tt} & Z^{EJ,t\phi} & Z^{EM,tt} & Z^{EM,t\phi} \\ Z^{EJ,\phi t} & Z^{EJ,\phi\phi} & Z^{EM,\phi t} & Z^{EM,\phi\phi} \\ Z^{HJ,tt} & Z^{HJ,t\phi} & Z^{HM,tt} & Z^{HM,t\phi} \\ Z^{HJ,\phi t} & Z^{HJ,\phi\phi} & Z^{HM,\phi t} & Z^{HM,\phi\phi} \end{bmatrix} \begin{bmatrix} I^{J,t} \\ I^{J,\phi} \\ I^{M,t} \\ I^{M,\phi} \end{bmatrix} = \begin{bmatrix} V^{E,t} \\ V^{E,\phi} \\ V^{H,t} \\ V^{H,\phi} \end{bmatrix} , \tag{7.99}$$

where the nMFIE is omitted for now.

7.5.1 Plane Wave Solution

Substitution of the matrix and vector sub-blocks for $\hat{\boldsymbol{\theta}}^i$-polarization into (7.99) yields as the solution for mode α

$$\begin{bmatrix} I^{J,t\theta^i} \\ I^{J,\phi\theta^i} \\ I^{M,t\theta^i} \\ I^{M,\phi\theta^i} \end{bmatrix}_\alpha = \begin{bmatrix} \mathrm{L}_E^{tt} & \mathrm{L}_E^{t\phi} & \mathrm{K}_E^{tt} & \mathrm{K}_E^{t\phi} \\ \mathrm{L}_E^{\phi t} & \mathrm{L}_E^{\phi\phi} & \mathrm{K}_E^{\phi t} & \mathrm{K}_E^{\phi\phi} \\ \mathrm{K}_H^{tt} & \mathrm{K}_H^{t\phi} & \mathrm{L}_H^{tt} & \mathrm{L}_H^{t\phi} \\ \mathrm{K}_H^{\phi t} & \mathrm{K}_H^{\phi\phi} & \mathrm{L}_H^{\phi t} & \mathrm{L}_H^{\phi\phi} \end{bmatrix}_\alpha^{-1} \begin{bmatrix} V^{E,t\theta^i} \\ V^{E,\phi\theta^i} \\ -V^{E,t\phi^i} \\ -V^{E,\phi\phi^i} \end{bmatrix}_\alpha . \tag{7.100}$$

Using (7.39) and (7.61), together with (7.91) and (7.92), the solution (7.100) for negative modes can be written as

$$\begin{bmatrix} I^{J,t\theta^i} \\ I^{J,\phi\theta^i} \\ I^{M,t\theta^i} \\ I^{M,\phi\theta^i} \end{bmatrix}_{-\alpha} = \begin{bmatrix} \mathrm{L}_E^{tt} & -\mathrm{L}_E^{t\phi} & -\mathrm{K}_E^{tt} & \mathrm{K}_E^{t\phi} \\ -\mathrm{L}_E^{\phi t} & \mathrm{L}_E^{\phi\phi} & \mathrm{K}_E^{\phi t} & -\mathrm{K}_E^{\phi\phi} \\ -\mathrm{K}_H^{tt} & \mathrm{K}_H^{t\phi} & \mathrm{L}_H^{tt} & -\mathrm{L}_H^{t\phi} \\ \mathrm{K}_H^{\phi t} & -\mathrm{K}_H^{\phi\phi} & -\mathrm{L}_H^{\phi t} & \mathrm{L}_H^{\phi\phi} \end{bmatrix}_{\alpha}^{-1} \begin{bmatrix} V^{E,t\theta^i} \\ -V^{E,\phi\theta^i} \\ V^{E,t\phi^i} \\ -V^{E,\phi\phi^i} \end{bmatrix}_{\alpha} . \tag{7.101}$$

Therefore,

$$\begin{bmatrix} I^{J,t\theta^i} \\ I^{J,\phi\theta^i} \\ I^{M,t\theta^i} \\ I^{M,\phi\theta^i} \end{bmatrix}_{-\alpha} = \begin{bmatrix} I^{J,t\theta^i} \\ -I^{J,\phi\theta^i} \\ -I^{M,t\theta^i} \\ I^{M,\phi\theta^i} \end{bmatrix}_{\alpha} , \tag{7.102}$$

where only $I^{J,t\theta^i}$ and $I^{M,\phi\theta^i}$ are nonzero for $\alpha = 0$. Similarly, for $\hat{\boldsymbol{\phi}}^i$-polarization, the solution to (7.99) for mode α is

$$\begin{bmatrix} I^{J,t\phi^i} \\ I^{J,\phi\phi^i} \\ I^{M,t\phi^i} \\ I^{M,\phi\phi^i} \end{bmatrix}_{\alpha} = \begin{bmatrix} \mathrm{L}_E^{tt} & \mathrm{L}_E^{t\phi} & \mathrm{K}_E^{tt} & \mathrm{K}_E^{t\phi} \\ \mathrm{L}_E^{\phi t} & \mathrm{L}_E^{\phi\phi} & \mathrm{K}_E^{\phi t} & \mathrm{K}_E^{\phi\phi} \\ \mathrm{K}_H^{tt} & \mathrm{K}_H^{t\phi} & \mathrm{L}_H^{tt} & \mathrm{L}_H^{t\phi} \\ \mathrm{K}_H^{\phi t} & \mathrm{K}_H^{\phi\phi} & \mathrm{L}_H^{\phi t} & \mathrm{L}_H^{\phi\phi} \end{bmatrix}_{\alpha}^{-1} \begin{bmatrix} V^{E,t\phi^i} \\ V^{E,\phi\phi^i} \\ V^{E,t\theta^i} \\ V^{E,\phi\theta^i} \end{bmatrix}_{\alpha} , \tag{7.103}$$

and for negative modes it is

$$\begin{bmatrix} I^{J,t\phi^i} \\ I^{J,\phi\phi^i} \\ I^{M,t\phi^i} \\ I^{M,\phi\phi^i} \end{bmatrix}_{-\alpha} = \begin{bmatrix} \mathrm{L}_E^{tt} & -\mathrm{L}_E^{t\phi} & -\mathrm{K}_E^{tt} & \mathrm{K}_E^{t\phi} \\ -\mathrm{L}_E^{\phi t} & \mathrm{L}_E^{\phi\phi} & \mathrm{K}_E^{\phi t} & -\mathrm{K}_E^{\phi\phi} \\ -\mathrm{K}_H^{tt} & \mathrm{K}_H^{t\phi} & \mathrm{L}_H^{tt} & -\mathrm{L}_H^{t\phi} \\ \mathrm{K}_H^{\phi t} & -\mathrm{K}_H^{\phi\phi} & -\mathrm{L}_H^{\phi t} & \mathrm{L}_H^{\phi\phi} \end{bmatrix}_{\alpha}^{-1} \begin{bmatrix} -V^{E,t\phi^i} \\ V^{E,\phi\phi^i} \\ V^{E,t\theta^i} \\ -V^{E,\phi\theta^i} \end{bmatrix}_{\alpha} . \tag{7.104}$$

Therefore,

$$\begin{bmatrix} I^{J,t\phi^i} \\ I^{J,\phi\phi^i} \\ I^{M,t\phi^i} \\ I^{M,\phi\phi^i} \end{bmatrix}_{-\alpha} = \begin{bmatrix} -I^{J,t\phi^i} \\ I^{J,\phi\phi^i} \\ I^{M,t\phi^i} \\ -I^{M,\phi\phi^i} \end{bmatrix}_{\alpha} , \tag{7.105}$$

where only $I^{J,\phi\phi^i}$ and $I^{M,t\phi^i}$ are nonzero for $\alpha = 0$.

7.5.1.1 Currents

For $\hat{\boldsymbol{\theta}}^i$-polarization, the electric and magnetic currents for basis function m can be written as

$$\mathbf{J}_m^{\theta^i}(\mathbf{r}) = \sum_{\alpha=-\infty}^{\infty} \left[I_{\alpha m}^{J,t\theta^i} f_m(t) \hat{\mathbf{t}}(\mathbf{r}) - I_{\alpha m}^{J,\phi\theta^i} f_m(t) \hat{\boldsymbol{\phi}}(\mathbf{r}) \right] e^{j\alpha\phi} , \tag{7.106}$$

and

$$\mathbf{M}_m^{\theta^i}(\mathbf{r}) = \sum_{\alpha=-\infty}^{\infty} \left[I_{\alpha m}^{M,t\theta^i} g_m(t)\hat{\mathbf{t}}(\mathbf{r}) - I_{\alpha m}^{M,\phi\theta^i} g_m(t)\hat{\boldsymbol{\phi}}(\mathbf{r}) \right] e^{j\alpha\phi} \,. \tag{7.107}$$

Using (7.102), these currents can be re-written using only positive modes as

$$\begin{aligned}\mathbf{J}_m^{\theta^i}(\mathbf{r}) =& I_{0m}^{J,t\theta^i} f_m(t)\hat{\mathbf{t}}(\mathbf{r}) \\ &+2\sum_{\alpha=1}^{\infty} \left[I_{\alpha m}^{J,t\theta^i} f_m(t)\cos(\alpha\phi)\hat{\mathbf{t}}(\mathbf{r}) - jI_{\alpha m}^{J,\phi\theta^i} f_m(t)\sin(\alpha\phi)\hat{\boldsymbol{\phi}}(\mathbf{r}) \right],\end{aligned} \tag{7.108}$$

and

$$\begin{aligned}\mathbf{M}_m^{\theta^i}(\mathbf{r}) =& - I_{0m}^{M,\phi\theta^i} g_m(t)\hat{\boldsymbol{\phi}}(\mathbf{r}) \\ &+2\sum_{\alpha=1}^{\infty} \left[jI_{\alpha m}^{M,t\theta^i} g_m(t)\sin(\alpha\phi)\hat{\mathbf{t}}(\mathbf{r}) - I_{\alpha m}^{M,\phi\theta^i} g_m(t)\cos(\alpha\phi)\hat{\boldsymbol{\phi}}(\mathbf{r}) \right].\end{aligned} \tag{7.109}$$

Similarly, for $\hat{\boldsymbol{\phi}}^{\,i}$-polarization, the currents are

$$\begin{aligned}\mathbf{J}_m^{\phi^i}(\mathbf{r}) =& - I_{0m}^{J,\phi\phi^i} f_m(t)\hat{\boldsymbol{\phi}}(\mathbf{r}) \\ &+2\sum_{\alpha=1}^{\infty} \left[jI_{\alpha m}^{J,t\phi^i} f_m(t)\sin(\alpha\phi)\hat{\mathbf{t}}(\mathbf{r}) - I_{\alpha m}^{J,\phi\phi^i} f_m(t)\cos(\alpha\phi)\hat{\boldsymbol{\phi}}(\mathbf{r}) \right],\end{aligned} \tag{7.110}$$

and

$$\begin{aligned}\mathbf{M}_m^{\phi^i}(\mathbf{r}) =& I_{0m}^{M,t\phi^i} g_m(t)\hat{\mathbf{t}}(\mathbf{r}) \\ &+2\sum_{\alpha=1}^{\infty} \left[I_{\alpha m}^{M,t\phi^i} g_m(t)\cos(\alpha\phi)\hat{\mathbf{t}}(\mathbf{r}) - jI_{\alpha m}^{M,\phi\phi^i} g_m(t)\sin(\alpha\phi)\hat{\boldsymbol{\phi}}(\mathbf{r}) \right].\end{aligned} \tag{7.111}$$

7.5.2 Scattered Field

The scattered near electric field in Region R_l can be obtained by substituting (7.4) and (7.7) into (3.108) and (3.112), and performing the integration over all basis functions in R_l. For general problems, the near field integrals must be performed numerically in the t and ϕ dimensions for each mode.

7.5.2.1 Scattered Far Fields

Using (7.108–7.111), the scattered far electric fields in the exterior free space region R_0 are obtained using (3.133), with the components of $\mathbf{A}(\mathbf{r})$ and $\mathbf{F}(\mathbf{r})$ given by

$$A_{**}(\mathbf{r}) = \mu_0 \frac{e^{-jk_0 r}}{4\pi r} \sum_{m=1}^{N} \int_{t_m} (\hat{\boldsymbol{\theta}}^s, \hat{\boldsymbol{\phi}}^s) \cdot \int_0^{2\pi} \mathbf{J}_m^{\theta^i,\phi^i}(\mathbf{r}') e^{jk_0 \hat{\mathbf{r}}^s \cdot \mathbf{r}'} \rho \, d\phi \, dt \tag{7.112}$$

and

$$F_{**}(\mathbf{r}) = \epsilon_0 \frac{e^{-jk_0 r}}{4\pi r} \sum_{m=1}^{N} \int_{t_m} (\hat{\boldsymbol{\theta}}^s, \hat{\boldsymbol{\phi}}^s) \cdot \int_0^{2\pi} \mathbf{M}_m^{\theta^i,\phi^i}(\mathbf{r}') e^{jk_0 \hat{\mathbf{r}}^s \cdot \mathbf{r}'} \rho \, d\phi \, dt \, , \quad (7.113)$$

where (θ^s, ϕ^s) are the spherical scattering angles, and $\hat{\mathbf{r}}^s$ the direction of scattering. The integration is performed over all basis functions in R_0. As before, the integrations versus ϕ in (7.112) and (7.113) can be performed analytically.

Let us focus on the innermost integral in (7.112) for basis function m, which has the form

$$(\hat{\boldsymbol{\theta}}^s, \hat{\boldsymbol{\phi}}^s) \cdot \int_0^{2\pi} \mathbf{J}_m^{\theta^i,\phi^i}(\mathbf{r}') e^{jk_0 \hat{\mathbf{r}}^s \cdot \mathbf{r}'} \rho \, d\phi \, . \quad (7.114)$$

The exponential term can be written as

$$e^{jk_0 \hat{\mathbf{r}}^s \cdot \mathbf{r}'} = e^{jk_0 z \cos\theta^s} e^{jk_0 \sin\theta^s \rho \cos(\phi - \phi^s)} \, . \quad (7.115)$$

Applying the dot products from before, the (θ^s, θ^i) term for modes $\alpha > 0$ is

$$\begin{aligned} & I_{\alpha m}^{J,t\theta^i} \int_0^{2\pi} e^{jk_0 \sin\theta^s \rho(t) \cos\phi} \cos(\alpha\phi + \alpha\phi^s) A(\theta^s, \phi, t) \, d\phi \\ + & I_{\alpha m}^{J,\phi\theta^i} \int_0^{2\pi} j e^{jk_0 \sin\theta^s \rho(t) \cos\phi} \sin\left(\alpha\phi + \alpha\phi^s\right) \sin\phi \cos\theta^s \, d\phi \, , \end{aligned} \quad (7.116)$$

where

$$A(\theta^s, \phi, t) = \cos\theta^s \sin\gamma(t) \cos\phi - \sin\theta^s \cos\gamma(t) \, , \quad (7.117)$$

and we have made the substitution $\phi = \phi + \phi^s$ due to the 2π periodicity. Now consider the first integral in (7.116). Using the identity

$$\cos(\alpha\phi + \alpha\phi^s) = \cos(\alpha\phi)\cos(\alpha\phi^s) - \sin(\alpha\phi)\sin(\alpha\phi^s) \, , \quad (7.118)$$

this integral becomes

$$\begin{aligned} I_1 = & \cos(\alpha\phi^s) \int_0^{2\pi} e^{jk_0 \sin\theta^s \rho(t) \cos\phi} \cos(\alpha\phi) A(\theta^s, \phi, t) \, d\phi \\ & - \sin(\alpha\phi^s) \int_0^{2\pi} e^{jk_0 \sin\theta^s \rho(t) \cos\phi} \sin(\alpha\phi) A(\theta^s, \phi, t) \, d\phi \, . \end{aligned} \quad (7.119)$$

The second term goes to zero by inspection. Using (7.79), the integral can then be written as

$$I_1 = \pi j^\alpha \Big[\cos\theta^s \sin\gamma(t) j \big[J_{\alpha+1}(x) - J_{\alpha-1}(x) \big] - 2 \sin\theta^s \cos\gamma(t) J_\alpha(x) \Big] \cos(\alpha\phi^s) \quad (7.120)$$

where $J_\alpha(x) = J_\alpha(k_0 \rho(t) \sin\theta^s)$. Using the identity

$$\sin(\alpha\phi + \alpha\phi^s) = \sin(\alpha\phi)\cos(\alpha\phi^s) + \cos(\alpha\phi)\sin(\alpha\phi^s) \quad (7.121)$$

the second integral in (7.116) becomes

$$I_2 = \cos(\alpha\phi^s)\cos\theta^s \int_0^{2\pi} je^{jk_0 \sin\theta^s \rho(t)\cos\phi} \sin(\alpha\phi)\sin\phi\, d\phi + \sin(\alpha\phi^s)\cos\theta^s \int_0^{2\pi} je^{jk_0 \sin\theta^s \rho(t)\cos\phi} \cos(\alpha\phi)\sin\phi\, d\phi\,. \tag{7.122}$$

The second term again is zero by inspection. The first term can be integrated by parts yielding

$$I_2 = \cos(\alpha\phi^s)\cos\theta^s \pi j^\alpha \frac{2\alpha}{x} J_\alpha(x)\,, \tag{7.123}$$

and again using (7.85) this becomes

$$I_2 = \pi j^\alpha \big[J_{\alpha+1}(x) + J_{\alpha-1}(x)\big]\cos\theta^s \cos(\alpha\phi^s)\,. \tag{7.124}$$

Combining the results, we see that the integrals have the same form as (7.87) and (7.88), where θ^i is replaced by θ^s. Thus, $A_{\theta\theta}$ can be written as

$$A_{\theta\theta}(\mathbf{r}) = \frac{C_A}{2} I_{0m}^{J,t\theta^i} V_0^{E,t\theta^s} + C_A \sum_{\alpha=1}^{\infty} \Big[I_{\alpha m}^{J,t\theta^i} V_\alpha^{E,t\theta^s} + I_{\alpha m}^{J,\phi\theta^i} V_\alpha^{E,\phi\theta^s}\Big]\cos(\alpha\phi^s)\,. \tag{7.125}$$

The other terms follow similarly, and are

$$A_{\phi\theta}(\mathbf{r}) = -jC_A \sum_{\alpha=1}^{\infty} \Big[I_{\alpha m}^{J,t\theta^i} V_\alpha^{E,t\phi^s} + I_{\alpha m}^{J,\phi\theta^i} V_\alpha^{E,\phi\phi^s}\Big]\sin(\alpha\phi^s)\,, \tag{7.126}$$

$$A_{\theta\phi}(\mathbf{r}) = jC_A \sum_{\alpha=1}^{\infty} \Big[I_{\alpha m}^{J,t\phi^i} V_\alpha^{E,t\theta^s} + I_{\alpha m}^{J,\phi\phi^i} V_\alpha^{E,\phi\theta^s}\Big]\sin(\alpha\phi^s)\,, \tag{7.127}$$

and

$$A_{\phi\phi}(\mathbf{r}) = -\frac{C_A}{2} I_{0m}^{J,\phi\phi^i} V_0^{E,\phi\phi^s} - C_A \sum_{\alpha=1}^{\infty} \Big[I_{\alpha m}^{J,t\phi^i} V_\alpha^{E,t\phi^s} + I_{\alpha m}^{J,\phi\phi^i} V_\alpha^{E,\phi\phi^s}\Big]\cos(\alpha\phi^s)\,, \tag{7.128}$$

where

$$C_A = \mu_0 \frac{e^{-jk_0 r}}{2\pi r}\,. \tag{7.129}$$

Similarly, the components of $\mathbf{F}(\mathbf{r})$ are

$$F_{\theta\theta}(\mathbf{r}) = jC_F \sum_{\alpha=1}^{\infty} \Big[I_{\alpha m}^{M,t\theta^i} V_\alpha^{E,t\theta^s} + I_{\alpha m}^{M,\phi\theta^i} V_\alpha^{E,\phi\theta^s}\Big]\sin(\alpha\phi^s)\,, \tag{7.130}$$

$$F_{\phi\theta}(\mathbf{r}) = -\frac{C_F}{2} I_{0m}^{M,\phi\theta^i} V_0^{E,\phi\phi^s} - C_F \sum_{\alpha=1}^{\infty} \Big[I_{\alpha m}^{M,t\theta^i} V_\alpha^{E,t\phi^s} + I_{\alpha m}^{M,\phi\theta^i} V_\alpha^{E,\phi\phi^s}\Big]\cos(\alpha\phi^s)\,, \tag{7.131}$$

$$F_{\theta\phi}(\mathbf{r}) = \frac{C_F}{2} I_{0m}^{M,t\phi^i} V_0^{E,t\theta^s} + C_F \sum_{\alpha=1}^{\infty} \left[I_{\alpha m}^{M,t\phi^i} V_\alpha^{E,t\theta^s} + I_{\alpha m}^{M,\phi\phi^i} V_\alpha^{E,\phi\theta^s} \right] \cos(\alpha\phi^s) \,, \quad (7.132)$$

and

$$F_{\phi\phi}(\mathbf{r}) = -jC_F \sum_{\alpha=1}^{\infty} \left[I_{\alpha m}^{M,t\phi^i} V_\alpha^{E,t\phi^s} + I_{\alpha m}^{M,\phi\phi^i} V_\alpha^{E,\phi\phi^s} \right] \sin(\alpha\phi^s) \,, \quad (7.133)$$

where

$$C_F = \epsilon_0 \eta_0 \frac{e^{-jk_0 r}}{2\pi r} \,. \quad (7.134)$$

Note that the right-hand side vectors V^{E,θ^i} and V^{E,ϕ^i} contain no references to the incident or observation angles ϕ^i or ϕ^s. For monostatic calculations, these vectors can be computed once per right-hand side and used to obtain the currents as well as the scattered fields.

7.6 nMFIE

The nMFIE (3.183) contains the $\hat{\mathbf{n}} \times \mathcal{L}$ and $\hat{\mathbf{n}} \times \mathcal{K}$ operators, which were discretized and tested via the MoM in (3.192) and (3.193). For the testing functions, we will use the electric testing functions in (7.11) and (7.12).

7.6.1 $\hat{\mathbf{n}} \times \mathcal{L}$ Operator

Substitution of the basis (7.8, 7.9) and testing (7.11, 7.12) functions into (3.193) yields a $2N \times 2N$ matrix of the form

$$Z^{nHM(l)} = \begin{bmatrix} \mathrm{nL}(\mathbf{f}_\beta^t, \mathbf{g}_\alpha^t) & \mathrm{nL}(\mathbf{f}_\beta^t, \mathbf{g}_\alpha^\phi) \\ \mathrm{nL}(\mathbf{f}_\beta^\phi, \mathbf{g}_\alpha^t) & \mathrm{nL}(\mathbf{f}_\beta^\phi, \mathbf{g}_\alpha^\phi) \end{bmatrix} = \begin{bmatrix} \mathrm{nL}^{tt} & \mathrm{nL}^{t\phi} \\ \mathrm{nL}^{\phi t} & \mathrm{nL}^{\phi\phi} \end{bmatrix} . \quad (7.135)$$

The elements of each sub-matrix block are given by

$$\begin{aligned} \mathrm{nL}_{mn}^{**} =& j\omega\epsilon_l \int_{\mathbf{f}_{\beta m}^{t,\phi}} \int_{\mathbf{g}_{\alpha n}^{t,\phi}} \left[\mathbf{f}_{\beta m}^{t,\phi}(\mathbf{r}) \times \hat{\mathbf{n}}_l(\mathbf{r}) \right] \cdot \int_{\mathbf{g}_{\alpha n}^{t,\phi}} \pm \mathbf{g}_{\alpha n}^{t,\phi}(\mathbf{r}') \frac{e^{-jk_l r}}{4\pi r} \, d\mathbf{r}' \Big] \, d\mathbf{r} \\ & - \frac{j}{\omega\mu_l} \int_{\mathbf{f}_{\beta m}^{t,\phi}} \nabla \cdot \left[\mathbf{f}_{\beta m}^{t,\phi}(\mathbf{r}) \times \hat{\mathbf{n}}_l(\mathbf{r}) \right] \int_{\mathbf{g}_{\alpha n}^{t,\phi}} \left[\nabla' \cdot \pm \mathbf{g}_{\alpha n}^{t,\phi}(\mathbf{r}') \right] \frac{e^{-jk_l r}}{4\pi r} \, d\mathbf{r}' \, d\mathbf{r} \,, \end{aligned} \quad (7.136)$$

where we have used (3.208) to re-distribute the cross products and differential operators.

7.6.1.1 nL Matrix Elements

Noting that

$$\hat{\mathbf{t}}(\mathbf{r}) \times \hat{\mathbf{n}}_l(\mathbf{r}) = \hat{\boldsymbol{\phi}}(\mathbf{r}) \quad (7.137)$$

and

$$\hat{\boldsymbol{\phi}}(\mathbf{r}) \times \hat{\mathbf{n}}_l(\mathbf{r}) = -\hat{\mathbf{t}}(\mathbf{r}) \,, \tag{7.138}$$

we see that (7.136) has the same form as (7.14). This allows us to write the nL sub-matrix elements in terms of the L sub-matrix elements as

$$\begin{bmatrix} \mathrm{nL}^{tt} & \mathrm{nL}^{t\phi} \\ \mathrm{nL}^{\phi t} & \mathrm{nL}^{\phi\phi} \end{bmatrix} = \eta_0 \frac{\epsilon_l}{\mu_l} \begin{bmatrix} \mathrm{L}^{\phi t} & \mathrm{L}^{\phi\phi} \\ -\mathrm{L}^{tt} & -\mathrm{L}^{t\phi} \end{bmatrix} . \tag{7.139}$$

Inspecting (7.139), we find that the relationship between positive and negative modes is

$$\begin{bmatrix} \mathrm{nL}^{tt} & \mathrm{nL}^{t\phi} \\ \mathrm{nL}^{\phi t} & \mathrm{nL}^{\phi\phi} \end{bmatrix}_{-\alpha} = \begin{bmatrix} -\mathrm{nL}^{tt} & \mathrm{nL}^{t\phi} \\ \mathrm{nL}^{\phi t} & -\mathrm{nL}^{\phi\phi} \end{bmatrix}_{\alpha} , \tag{7.140}$$

which are the same properties found in the K matrix.

7.6.2 $\hat{\mathbf{n}} \times \mathcal{K}$ Operator

Substitution of the basis (7.5, 7.6) and testing (7.11, 7.12) functions into (3.192) yields a matrix of the form

$$Z^{nHJ(l)} = \begin{bmatrix} \mathrm{nK}(\mathbf{f}^t_\beta, \mathbf{f}^t_\alpha) & \mathrm{nK}(\mathbf{f}^t_\beta, \mathbf{f}^\phi_\alpha) \\ \mathrm{nK}(\mathbf{f}^\phi_\beta, \mathbf{f}^t_\alpha) & \mathrm{nK}(\mathbf{f}^\phi_\beta, \mathbf{f}^\phi_\alpha) \end{bmatrix} = \begin{bmatrix} \mathrm{nK}^{tt} & \mathrm{nK}^{t\phi} \\ \mathrm{nK}^{\phi t} & \mathrm{nK}^{\phi\phi} \end{bmatrix} , \tag{7.141}$$

where in Region R_l, the elements of each sub-matrix block are given by

$$\begin{aligned} \mathrm{nK}^{**}_{mn} =& \frac{1}{2} \int_{\mathbf{f}^{t,\phi}_{\beta m}, \mathbf{f}^{t,\phi}_{\alpha n}} \mathbf{f}^{t,\phi}_{\beta m}(\mathbf{r}) \cdot \pm \mathbf{f}^{t,\phi}_{\alpha n}(\mathbf{r}) \, d\mathbf{r} \\ &+ \int_{\mathbf{f}^{t,\phi}_{\beta m}} \mathbf{f}^{t,\phi}_{\beta m}(\mathbf{r}) \cdot \hat{\mathbf{n}}(\mathbf{r}) \times \int_{\mathbf{f}^{t,\phi}_{\alpha n}} \Big[(\mathbf{r} - \mathbf{r}') \times \pm \mathbf{f}^{t,\phi}_{\alpha n}(\mathbf{r}') \Big] \frac{1 + jk_l r}{4\pi r^3} e^{-jk_l r} \, d\mathbf{r}' d\mathbf{r} \,. \end{aligned} \tag{7.142}$$

7.6.2.1 nK Matrix Elements

In evaluating the sub-matrix elements in (7.142), we again use (7.42–7.47) and note that

$$\hat{\mathbf{t}}(\mathbf{r}) \cdot \hat{\mathbf{n}}(\mathbf{r}) \times \Big[(\mathbf{r} - \mathbf{r}') \times \mathbf{f}(\mathbf{r}') \Big] = \hat{\boldsymbol{\phi}}(\mathbf{r}) \cdot \Big[(\mathbf{r} - \mathbf{r}') \times \mathbf{f}(\mathbf{r}') \Big] \tag{7.143}$$

and

$$\hat{\boldsymbol{\phi}}(\mathbf{r}) \cdot \hat{\mathbf{n}}(\mathbf{r}) \times \Big[(\mathbf{r} - \mathbf{r}') \times \mathbf{f}(\mathbf{r}') \Big] = -\hat{\mathbf{t}}(\mathbf{r}) \cdot \Big[(\mathbf{r} - \mathbf{r}') \times \mathbf{f}(\mathbf{r}') \Big], \tag{7.144}$$

which have the same form as (7.48–7.51). Thus, we can write the nK sub-matrix elements in terms of the K sub-matrix elements as

$$\begin{bmatrix} \mathrm{nK}^{tt} & \mathrm{nK}^{t\phi} \\ \mathrm{nK}^{\phi t} & \mathrm{nK}^{\phi\phi} \end{bmatrix} = \frac{1}{\eta_0} \begin{bmatrix} -\mathrm{K}^{\phi t} - \tilde{\mathrm{K}} & -\mathrm{K}^{\phi\phi} \\ \mathrm{K}^{tt} & \mathrm{K}^{t\phi} + \tilde{\mathrm{K}} \end{bmatrix} . \tag{7.145}$$

Inspecting (7.145), we find that the relationship between positive and negative modes is

$$\begin{bmatrix} \mathrm{nK}^{tt} & \mathrm{nK}^{t\phi} \\ \mathrm{nK}^{\phi t} & \mathrm{nK}^{\phi\phi} \end{bmatrix}_{-\alpha} = \begin{bmatrix} \mathrm{nK}^{tt} & -\mathrm{nK}^{t\phi} \\ -\mathrm{nK}^{\phi t} & \mathrm{nK}^{\phi\phi} \end{bmatrix}_{\alpha} , \tag{7.146}$$

which are the same properties found in the L matrix.

7.6.3 Excitation

Right-hand side vector elements for the nMFIE can be obtained by substituting the testing functions $\mathbf{f}_{\alpha m}^{t,\phi}(\mathbf{r})$ into (3.196). This yields a column vector of the form

$$V^{nH(l)} = \begin{bmatrix} V^{nH(l),t} \\ V^{nH(l),\phi} \end{bmatrix}. \tag{7.147}$$

The individual elements are given by

$$V_m^{nH(l),(t,\phi)} = \int_{T_m} \int_0^{2\pi} \mathbf{f}_{\alpha m}^{t,\phi}(\mathbf{r}) \cdot \left[\hat{\mathbf{n}}_l(\mathbf{r}) \times \mathbf{H}^i(\mathbf{r})\right] \rho \, d\phi \, dt \, , \tag{7.148}$$

where $\mathbf{H}^i(\mathbf{r})$ is the impressed magnetic field. As with the EFIE and MFIE, this can be evaluated analytically in the ϕ dimension for incident plane waves.

7.6.3.1 Plane Wave Excitation

While the components of the incident magnetic field are the same as in Section 7.4.1.1, we must now take into account the presence of $\hat{\mathbf{n}}(\mathbf{r})$ in (7.148). Making the following substitutions

$$\hat{\mathbf{t}}(\mathbf{r}) = \sin\gamma\cos\phi\hat{\mathbf{x}} + \sin\gamma\sin\phi\hat{\mathbf{y}} + \cos\gamma\hat{\mathbf{z}} \, , \tag{7.149}$$

$$\hat{\boldsymbol{\phi}}(\mathbf{r}) = -\sin\phi\hat{\mathbf{x}} + \cos\phi\hat{\mathbf{y}} \, , \tag{7.150}$$

$$\hat{\mathbf{n}}(\mathbf{r}) = \cos\gamma\cos\phi\hat{\mathbf{x}} + \cos\gamma\sin\phi\hat{\mathbf{y}} - \sin\gamma\hat{\mathbf{z}} \, , \tag{7.151}$$

and using (7.66) and (7.67), we find that

$$\hat{\mathbf{t}}(\mathbf{r}) \cdot \left[\hat{\mathbf{n}}(\mathbf{r}) \times \hat{\boldsymbol{\theta}}^i\right] = -\cos\theta^i \sin\phi \, , \tag{7.152}$$

$$\hat{\boldsymbol{\phi}}(\mathbf{r}) \cdot \left[\hat{\mathbf{n}}(\mathbf{r}) \times \hat{\boldsymbol{\theta}}^i\right] = \cos\gamma\sin\theta^i - \sin\gamma\cos\theta^i\cos\phi \, , \tag{7.153}$$

$$\hat{\mathbf{t}}(\mathbf{r}) \cdot \left[\hat{\mathbf{n}}(\mathbf{r}) \times -\hat{\boldsymbol{\phi}}^i\right] = -\cos\phi \, , \tag{7.154}$$

$$\hat{\boldsymbol{\phi}}(\mathbf{r}) \cdot \left[\hat{\mathbf{n}}(\mathbf{r}) \times -\hat{\boldsymbol{\phi}}^i\right] = \sin\gamma\sin\phi \, , \tag{7.155}$$

where we have again set $\phi^i = 0$ for convenience. We immediately note that these results are identical to those in (7.68–7.71), and so the elements of $V^{nH(l)}$ can be written in terms of $V^{E(l)}$. In particular,

$$V^{nH,\theta^i} = \begin{bmatrix} V^{nH,t\theta^i} \\ V^{nH,\phi\theta^i} \end{bmatrix} = \frac{1}{\eta_0} \begin{bmatrix} -V^{E,\phi\phi^i} \\ V^{E,t\phi^i} \end{bmatrix}, \tag{7.156}$$

and

$$V^{nH,\phi^i} = \begin{bmatrix} V^{nH,t\phi^i} \\ V^{nH,\phi\phi^i} \end{bmatrix} = \frac{1}{\eta_0} \begin{bmatrix} V^{E,\phi\theta^i} \\ -V^{E,t\theta^i} \end{bmatrix}. \tag{7.157}$$

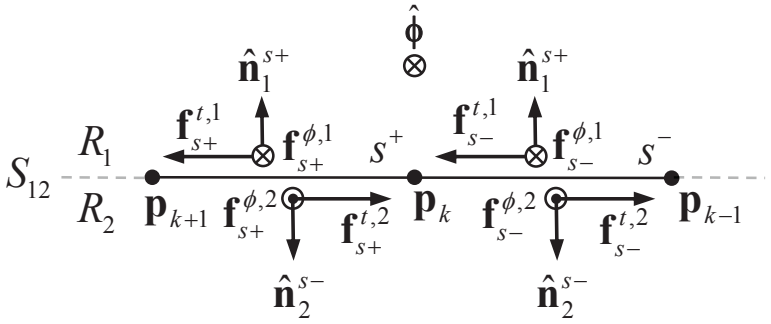


Figure 7.2: Basis Function Orientation for BoR Problems

7.6.3.2 Plane Wave Solution

Referring again to (7.87–7.90), we find that the relationship between positive and negative modes is

$$\begin{bmatrix} V^{nH,t\theta^i} \\ V^{nH,\phi\theta^i} \end{bmatrix}_{-\alpha} = \begin{bmatrix} V^{nH,t\theta^i} \\ -V^{nH,\phi\theta^i} \end{bmatrix}_{\alpha}, \tag{7.158}$$

and

$$\begin{bmatrix} V^{nH,t\phi^i} \\ V^{nH,\phi\phi^i} \end{bmatrix}_{-\alpha} = \begin{bmatrix} -V^{nH,t\phi^i} \\ V^{nH,\phi\phi^i} \end{bmatrix}_{\alpha}, \tag{7.159}$$

which are the same properties observed in (7.91) and (7.92). Noting that the nL and nK matrix have the same behavior as the K and L matrix for negative modes, as well as the EFIE and nMFIE right-hand side vectors, the EFIE and nMFIE can be combined in (7.99) to form the CFIE (3.184) with no additional modifications.

7.7 Numerical Discretization

A common way to describe a BoR is a piecewise linear approximation of the bounding curve in the xz plane ($\phi = 0$). The curve is divided into N segments with $N + 1$ unique endpoints, where the segments need not be of equal length. Each segment, when rotated 360 degrees about $\hat{\mathbf{z}}$, sweeps out an annulus on the surface. To define the longitudinal and normal vectors on each segment, we again use a right-handed rule (see Section 6.15). Consider the triangle function with support on segments $s+$ and $s-$, whose endpoints comprise $(\mathbf{p}_{k-1}, \mathbf{p}_k, \mathbf{p}_{k+1})$. These segments reside on the interface S_{12} between dielectric regions R_1 and R_2, as shown in Figure 7.2. Let us define the unit vectors

$$\hat{\mathbf{t}}^{s+} = \frac{\mathbf{p}_{k+1} - \mathbf{p}_k}{|\mathbf{p}_{k+1} - \mathbf{p}_k|}, \tag{7.160}$$

$$\hat{\mathbf{t}}^{s-} = \frac{\mathbf{p}_k - \mathbf{p}_{k-1}}{|\mathbf{p}_k - \mathbf{p}_{k-1}|}. \tag{7.161}$$

Following Section 6.2.1, we define R_1 as the "positive" side of the interface. On this side, the vectors normal to each segment are then

$$\hat{\mathbf{n}}_1^{s+} = \hat{\boldsymbol{\phi}} \times \hat{\mathbf{t}}^{s+} \,, \tag{7.162}$$

$$\hat{\mathbf{n}}_1^{s-} = \hat{\boldsymbol{\phi}} \times \hat{\mathbf{t}}^{s-} \,. \tag{7.163}$$

We then define the longitudinal basis vectors on each segment in R_1 as

$$\hat{\mathbf{f}}_{s+}^{t,1} = \hat{\mathbf{t}}^{s+} \,, \tag{7.164}$$

$$\hat{\mathbf{f}}_{s-}^{t,1} = \hat{\mathbf{t}}^{s-} \,, \tag{7.165}$$

and the azimuthal basis vectors as

$$\hat{\mathbf{f}}_{s+}^{\phi,1} = \hat{\boldsymbol{\phi}} \,, \tag{7.166}$$

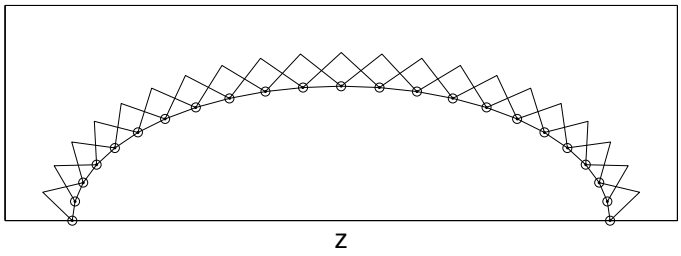
$$\hat{\mathbf{f}}_{s-}^{\phi,1} = \hat{\boldsymbol{\phi}} \,. \tag{7.167}$$

On the opposite or "negative" side of the interface in R_2, the direction of the normal vectors and the basis functions in R_1 are then reversed, as shown in Figure 7.2. All currents have opposite orientations on each side of the interface, and for the longitudinally oriented currents, Kirchhoff's current law is satisfied at p_k. To facilitate this orientation, the (x, z) locations of the segment endpoints are typically stored in a *boundary* or *points* structure, such that the longitudinal vectors are piecewise continuous between segments.

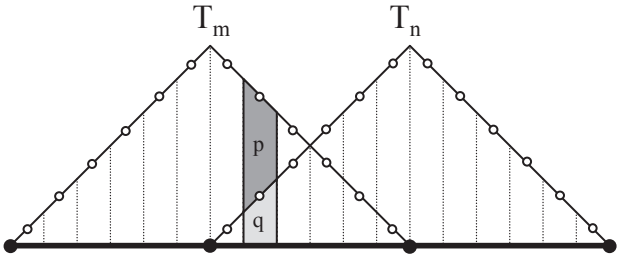
Other treatments [1, 2, 4] use triangle functions that span $2d$ boundary segments with d segments per half-triangle. Triangles are assigned a constant value on each segment, and integrations in the t dimension are evaluated using a centroidal approximation. Therein, the use of two segments per half-triangle is suggested, though this choice was likely due to the computer limitations of the time. Our treatment here uses triangle functions as defined in Section 2.3.2, with triangles assigned to no more than two segments, and Gaussian quadratures on segments in the t dimension. This assignment is illustrated on a simple, closed ellipse in Figure 7.3a.

When computing the integrals (7.35–7.37) and (7.58–7.60), special treatment is needed when $\mathbf{r} = \mathbf{r}'$. This occurs on overlapping segments when $t = t'$, as illustrated in Figure 7.3b. In this case, an alternative expression for r should be used when computing the integral versus ϕ', which is [1]

$$r = \sqrt{(\Delta_s/4)^2 + 2\rho^2[1 - \cos\phi']} \,. \tag{7.168}$$



(a) Assignment of Triangle Functions



(b) Sub-Segment Discretization

Figure 7.3: Triangle Functions on a BoR

7.8 Notes on Software Implementation

In this section we will discuss software implementation of the MoM/BoR technique.

7.8.1 Geometry Processing and Basis Function Assignment

Our approach for the description and processing of BoR geometry is to specify the segments on each material interface as a separate list of one or more boundary segments. Segments that are too long versus the operating wavelength can be subdivided automatically prior to processing. Segments are then read in, endpoints analyzed, and coincident endpoints identified as junctions and combined. The vector orientation of surface normals at each junction is done in a 2D sense, similar to the approach found in Section 8.7.1.3. The assignment and orientation of basis functions at endpoints and junctions is discussed in more detail in Section 7.10.

7.8.2 Parallelization

The MoM/BoR formulation produces a system matrix of relatively modest size. Therefore, it is convenient to allocate separate matrix storage space for each compute thread, and to allow each thread to work independently from the others. Each thread then performs the matrix fill, factorization, and calculation of the scattered fields across all excitations and scattering angles for a unique mode. Threads can select mode numbers

based on their thread index and size of the thread pool, or simply from modes not already processed. This scheme is equally well suited for shared memory and distributed memory (MPI) systems.

7.8.3 Convergence

In practice, the calculation for a given frequency would be halted at a maximum mode number. However, as the amplitude of the scattered field tends to decrease with mode number, it is likely that the calculation may converge to an accurate solution fairly quickly. One way to determine if convergence has been reached is to apply a threshold to the amplitude of the radiated/scattered field for each scattering angle. If the amplitudes across all angles fall below this threshold, computations for that frequency can be considered as converged. This method is especially useful in monostatic RCS computations due to the many right-hand side operations that can be skipped, increasing the efficiency of the code for larger problems.

7.9 Examples

In this section we will use the MoM/BoR approach developed so far in this chapter to compute the RCS of several test articles. We will first consider a series of conducting, dielectric, and coated spheres, then a set of benchmark targets that were constructed and measured by the Electromagnetic Code Consortium (EMCC) [5]. We will then look at more complicated configurations, such as conducting and partially conducting (coated) reentry vehicles (RVs). The numerical results in this section were computed using a software called *Galaxy*, which is part of the *lucernhammer* suite of radar cross section codes. *Galaxy* is written in the C++ programming language, and is parallelized using threads. Unless otherwise specified, the BoR treatment employs 5 subsegments per half-triangle for integration in the t dimension, PMCHWT is applied on dielectrics, and the CFIE is used on closed conductors with $\alpha = 0.5$.

7.9.1 Spheres

Spheres are excellent benchmark geometries for computational electromagnetic codes, as analytic solutions for their scattering of plane waves are known. Let us assume that there is a plane wave traveling in the $-\hat{\mathbf{z}}$ direction with an $\hat{\mathbf{x}}$-oriented electric field of unit amplitude. The exact value for the scattered far electric field is [6]

$$\mathbf{E}^s(\theta^s, \phi^s) = \frac{e^{-jk_0 r}}{k_0 r}\left[\cos\phi^s S_1(\theta^s)\,\hat{\boldsymbol{\theta}} - \sin\phi^s S_2(\theta^s)\,\hat{\boldsymbol{\phi}}\right], \tag{7.169}$$

where

$$S_1(\theta) = \sum_{n=1}^{\infty} j^{n+1}\left[A_n \frac{P_n^1(\cos\theta)}{\sin\theta} - jB_n \frac{d}{d\theta}P_n^1(\cos\theta)\right], \tag{7.170}$$

$$S_2(\theta) = \sum_{n=1}^{\infty} j^{n+1}\left[A_n \frac{d}{d\theta}P_n^1(\cos\theta) - jB_n \frac{P_n^1(\cos\theta)}{\sin\theta}\right], \tag{7.171}$$

and $P_n^1(\cos\theta)$ is the associated Legendre polynomial of degree n and order 1. In practice, the sums in (7.170) and (7.171) are truncated after a finite number of modes, and the recurrence relationships in [3] are used to compute the associated Legendre polynomials of higher order. The coefficients A_n and B_n differ depending on whether the sphere is conducting, or fully or partially dielectric. We will consider examples of each in this section.

7.9.1.1 Conducting Sphere

For a conducting sphere of radius a, the coefficients A_n and B_n are

$$A_n = -j^n \frac{2n+1}{n(n+1)} \frac{j_n(k_0 a)}{h_n^{(2)}(k_0 a)} \,, \tag{7.172}$$

and

$$B_n = j^{n+1} \frac{2n+1}{n(n+1)} \frac{\big[k_0 a\, j_n(k_0 a)\big]'}{\big[k_0 a\, h_n^{(2)}(k_0 a)\big]'} \,, \tag{7.173}$$

where $j_n(k_0 a)$ and $h_n^{(2)}(k_0 a)$ are the spherical Bessel function of the first kind, and spherical Hankel function of the second kind, of order n, and the primes indicate differentiation with respect to $k_0 a$ [6]. Spherical Bessel functions can be written as

$$f_n(x) = \sqrt{\frac{\pi}{2x}} F_{n+1/2}(x) \,, \tag{7.174}$$

where $f_n(x)$ is a spherical Bessel function of the first or second kind ($j_n(x)$ and $y_n(x)$, respectively), and $F_n(x)$ is a regular Bessel function of the first or second kind ($J_n(x)$ and $Y_n(x)$, respectively). The spherical Hankel function is

$$h_n^{(2)}(x) = j_n(x) - j y_n(x) \,. \tag{7.175}$$

The derivatives of the spherical Bessel functions are

$$\frac{d}{dx}\big[x f_n(x)\big] = \sqrt{\frac{\pi}{2x}}\Big[x F_{n-1/2}(x) - n F_{n+1/2}(x)\Big] \,. \tag{7.176}$$

7.9.1.1.1 MoM System Matrix

The conducting sphere comprises a single bounding curve S_{01} between the free space region R_0 and the interior conducting region R_1. Applying the CFIE yields a linear system of the form

$$\Big[\alpha_c Z^{EJ} + (1-\alpha_c) Z^{nHJ}\Big]\Big[I^J\Big] = \Big[\alpha_c V^E + (1-\alpha_c) V^{nH}\Big], \tag{7.177}$$

where

$$Z^{EJ} = \begin{bmatrix} \mathrm{L}\big(\mathbf{f}_{S_{01}}^t, \mathbf{f}_{S_{01}}^t, R_0\big) & \mathrm{L}\big(\mathbf{f}_{S_{01}}^t, \mathbf{f}_{S_{01}}^\phi, R_0\big) \\ \mathrm{L}\big(\mathbf{f}_{S_{01}}^\phi, \mathbf{f}_{S_{01}}^t, R_0\big) & \mathrm{L}\big(\mathbf{f}_{S_{01}}^\phi, \mathbf{f}_{S_{01}}^\phi, R_0\big) \end{bmatrix}, \tag{7.178}$$

and

$$Z^{nHJ} = \begin{bmatrix} \mathrm{nK}\big(\mathbf{f}^t_{S_{01}}, \mathbf{f}^t_{S_{01}}, R_0\big) & \mathrm{nK}\big(\mathbf{f}^t_{S_{01}}, \mathbf{f}^\phi_{S_{01}}, R_0\big) \\ \mathrm{nK}\big(\mathbf{f}^\phi_{S_{01}}, \mathbf{f}^t_{S_{01}}, R_0\big) & \mathrm{nK}\big(\mathbf{f}^\phi_{S_{01}}, \mathbf{f}^\phi_{S_{01}}, R_0\big) \end{bmatrix} . \tag{7.179}$$

The notation $\mathrm{X}\big(\mathbf{a}_{S_l}, \mathbf{b}_{S_m}, R_l\big)$ indicates that X is evaluated in R_l for the testing and basis functions **a** and **b** that reside on the boundaries S_l and S_m, respectively. The right-hand side vectors are

$$V^E = \begin{bmatrix} V^E\big(\mathbf{f}^t_{S_{01}}, R_0\big) \\ V^E\big(\mathbf{f}^\phi_{S_{01}}, R_0\big) \end{bmatrix} , \tag{7.180}$$

and

$$V^{nH} = \begin{bmatrix} V^{nH}\big(\mathbf{f}^t_{S_{01}}, R_0\big) \\ V^{nH}\big(\mathbf{f}^\phi_{S_{01}}, R_0\big) \end{bmatrix} , \tag{7.181}$$

and the solution vector is

$$I^J = \begin{bmatrix} I^{J,t}_{S_{01}} \\ I^{J,\phi}_{S_{01}} \end{bmatrix} . \tag{7.182}$$

7.9.1.1.2 Monostatic RCS versus Frequency

We first compute the monostatic RCS of a conducting sphere of radius 0.5 meters for frequencies between 10 MHz and 2 GHz. For the Mie terms (7.170) and (7.171) we truncate the summation after 40 modes, and for the BoR bounding curve, we use 180 segments of equal length. In Figures 7.4a and 7.4b we compare the Mie series RCS to that of the EFIE and nMFIE, respectively. The comparisons are good at lower frequencies, though discrepancies begin to appear as frequency increases, particularly in the nMFIE results. These correspond to the internal resonances of the discretized BoR. Figure 7.5a shows the results obtained using the CFIE, where the comparison is very good and the resonance problems have been eliminated, as expected.

7.9.1.1.3 Range Profile

We next compare the *range profiles* of the sphere using the backscattered field from the CFIE and Mie series. The range profile is a time domain representation of the electromagnetic signature and can be used to localize the effective scattering centers of a target in the down-range dimension. Given an array S of complex-valued backscattered electric field samples over a range of evenly spaced frequencies f_{min} to f_{max}, the range profile R is

$$R = \mathrm{IFFT}(S) . \tag{7.183}$$

In radar signal processing, this is often referred to as *pulse compression* or *matched filtering*. More specifically, (7.183) is very similar to what is known as *stretch processing*, or "one-pass" pulse compression [7]. The range resolution of the time-domain waveform is

$$\Delta_R = \frac{c}{2B} , \tag{7.184}$$

where the operating bandwidth B is

$$B = f_{max} - f_{min} \; . \tag{7.185}$$

In order to reduce sidelobes in the range domain, a window function is usually applied to the frequency domain samples prior to performing the FFT. A commonly used window function is the *Hamming window* [8], which comprises the N element array W with elements given by

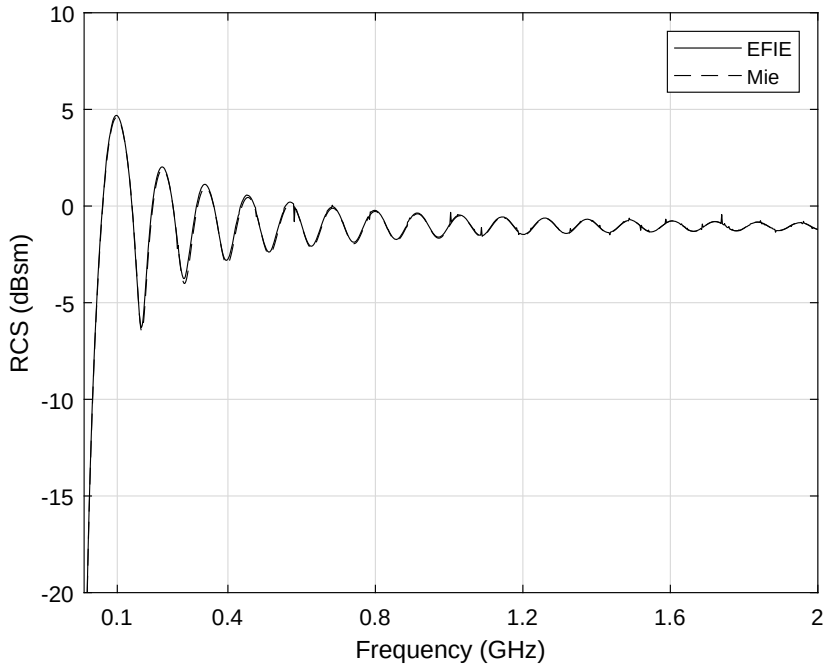
$$W_{k+1} = 0.54 - 0.46 \cos \left[\frac{2\pi k}{N-1} \right] \qquad k = 0, \ldots, N-1 \; . \tag{7.186}$$

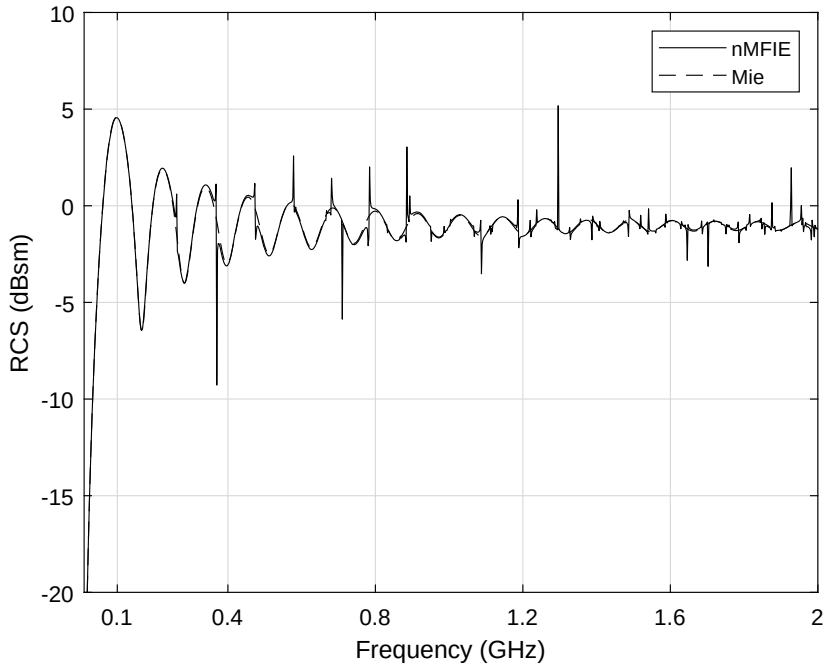
This windowing operation decreases the sidelobes at the expense of decreased range resolution. In particular, the Hamming window yields a first sidelobe level of approximately -40 dB, at the expense of increasing the half-power width of the main lobe by around 40%.

Figure 7.5b depicts the monostatic range profiles of the CFIE and Mie series computed from the complex-valued scattered field sampled from 1 to 2 GHz. A total of 32 samples were used, and the 1 GHz bandwidth yields in a range resolution of approximately 15 cm, which is decreased by the application of a Hamming window. Positive range in this figure represents the down-range direction. Noticeable immediately at a range of -0.5 m is the bright specular reflection from the sphere. Located slightly further down-range, at an amplitude of around -28 dB, is the well-known creeping wave response. This results from electromagnetic energy that originates at the shadow boundary and travels along the surface on the shadowed side of the sphere, returning eventually to the direction of incidence. The results are virtually indistinguishable.

7.9.1.1.4 Bistatic RCS

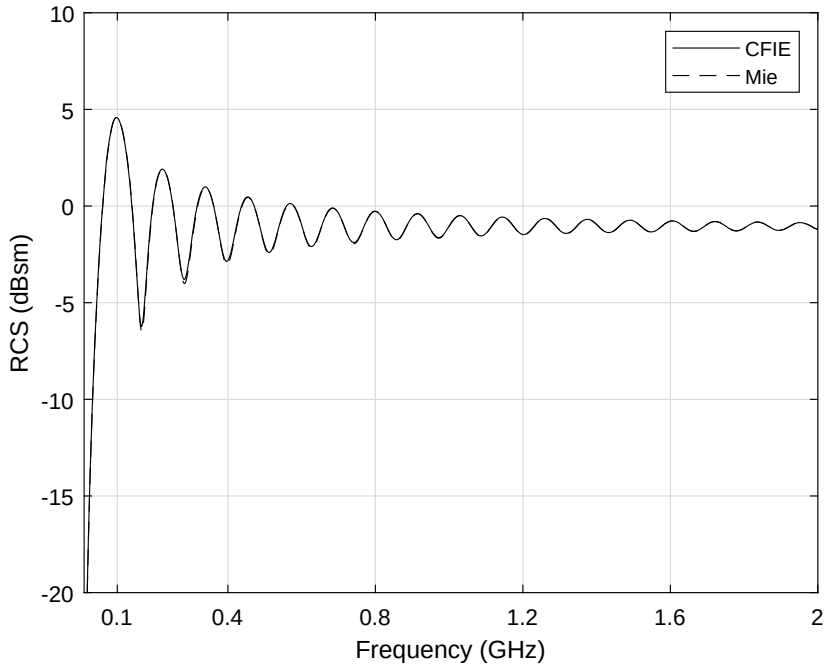
The bistatic RCS of the sphere is another commonly used benchmark. We retain the same geometry and simulation parameters as before, and consider the bistatic RCS at 0.3, 1.0 and 2.0 GHz, for bistatic angles between 0 and 180 degrees. The results from the CFIE are compared to the Mie series in Figures 7.6a–7.6f. The comparison is fairly good at 0.3 GHz, and at 1.0 and 2.0 GHz, the results are indistinguishable.

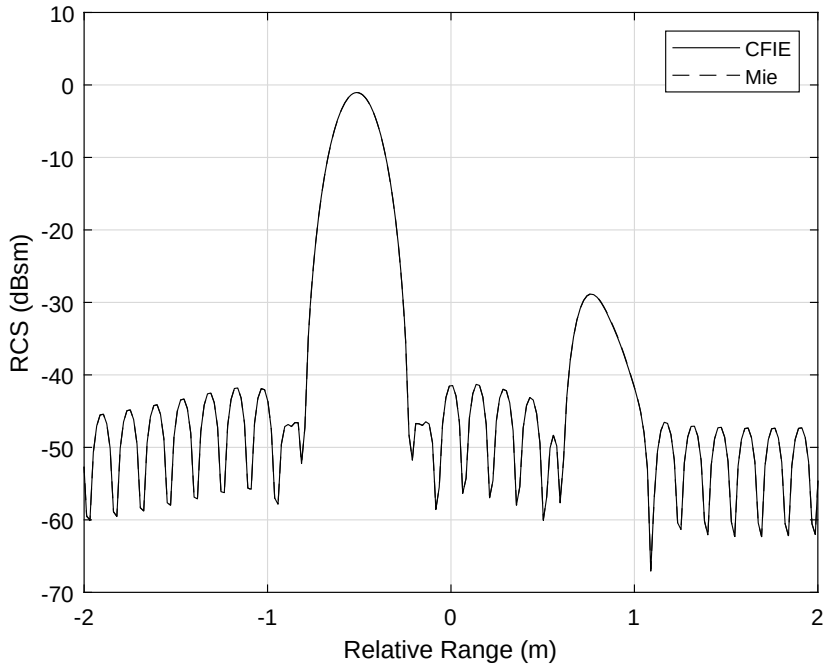




(b) RCS vs. Frequency: nMFIE vs. Mie

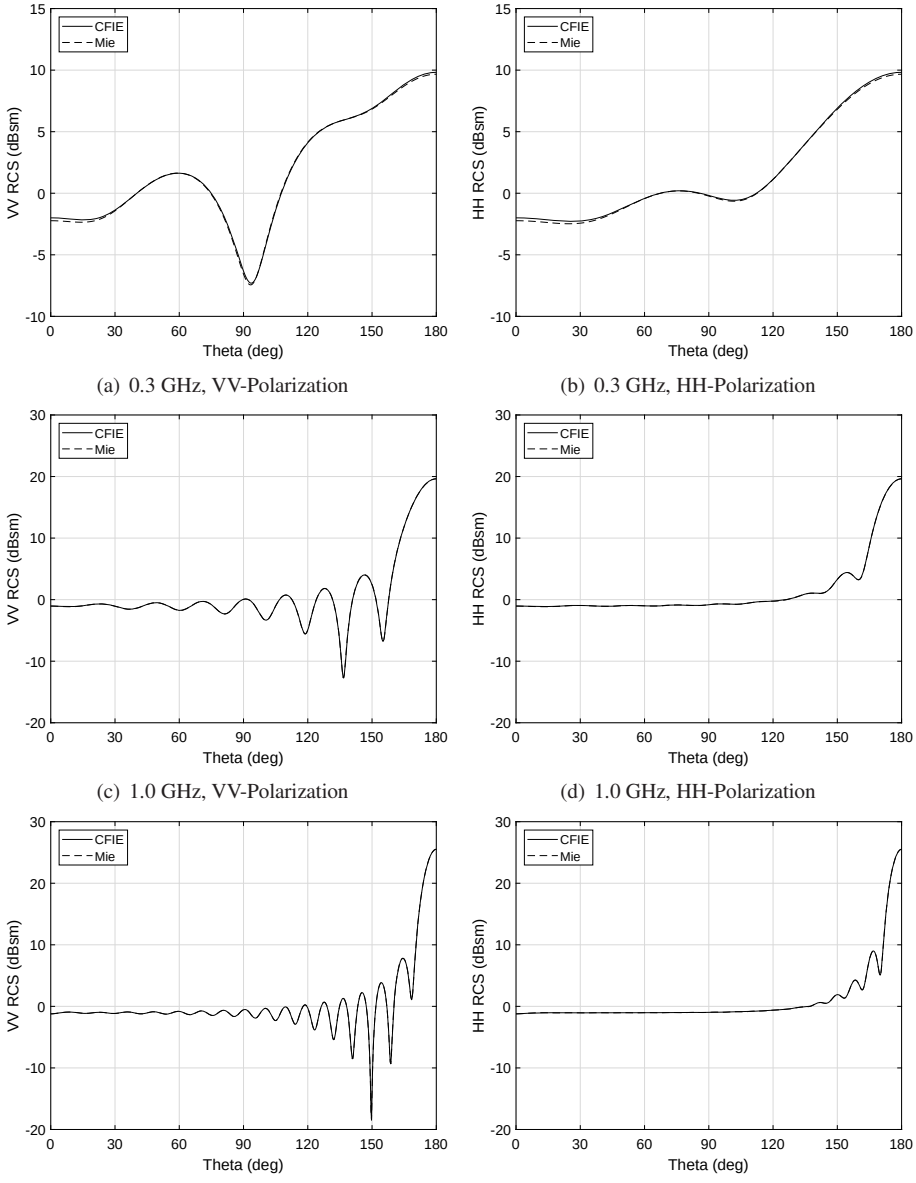
Figure 7.4: Conducting Sphere: EFIE and nMFIE vs. Mie





(b) Range Profile

Figure 7.5: Conducting Sphere: CFIE vs. Mie



(a) 0.3 GHz, VV-Polarization

(b) 0.3 GHz, HH-Polarization

(c) 1.0 GHz, VV-Polarization

(d) 1.0 GHz, HH-Polarization

(e) 2.0 GHz, VV-Polarization

(f) 2.0 GHz, HH-Polarization

Figure 7.6: Conducting Sphere: Bistatic RCS

7.9.1.2 Stratified Sphere

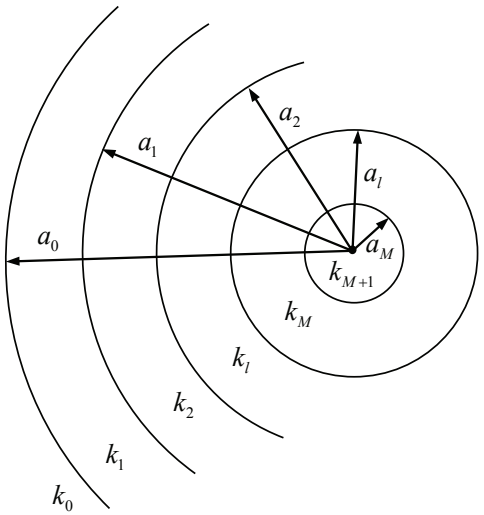


Figure 7.7: Geometry of an M-Layer Stratified Sphere

We next consider the radially stratified geometry of Figure 7.7, where the core may or may not be conducting. The Mie series coefficients [1] for this configuration are [6]

$$A_n = -j^n \frac{2n+1}{n(n+1)} \frac{k_0 a_0 j_n(k_0 a_0) + j Z_n(k_0 a_0) \big[k_0 a_0 j_n(k_0 a_0)\big]'}{k_0 a_0 h_n^{(2)}(k_0 a_0) + j Z_n(k_0 a_0) \big[k_0 a_0 h_n^{(2)}(k_0 a_0)\big]'} \tag{7.187}$$

and

$$B_n = j^{n+1} \frac{2n+1}{n(n+1)} \frac{k_0 a_0 j_n(k_0 a_0) + j Y_n(k_0 a_0) \big[k_0 a_0 j_n(k_0 a_0)\big]'}{k_0 a_0 h_n^{(2)}(k_0 a_0) + j Y_n(k_0 a_0) \big[k_0 a_0 h_n^{(2)}(k_0 a_0)\big]'} , \tag{7.188}$$

where a_0 is the outermost radius of the sphere. $Z_n(k_0 a_0)$ and $Y_n(k_0 a_0)$ are called the modal surface impedance and admittance, respectively, and depend on the composition of the sphere. We consider the general case in this section, which can be applied to dielectric as well as coated spheres with many layers. Calculation of these coefficients is as follows: First, we define the surface impedance at the interface of radius a_l as Z_n^l. The impedance Z_n^M between the core and the first layer is then determined, and from Z_n^M, the impedance Z_n^{M-1} at the second interface from the center is found. This process is repeated until Z_n^0 at the outer surface is obtained. Then,

$$Z_n(k_0 a_0) = \frac{j}{\eta_0} Z_n^0 \tag{7.189}$$

[1] There is an error in the leading coefficient on the right-hand side of (3.4-2) in [6], which has been corrected here.

and

$$Y_n(k_0 a_0) = j\eta_0 Y_n^0 \,, \tag{7.190}$$

where the admittance Y_n^0 is found from Y_n^M using a similar procedure. For the iterative procedure, we first make the following definitions

$$P_n(x) = \frac{x j_n(x)}{\left[x j_n(x)\right]'} \,, \tag{7.191}$$

$$Q_n(x) = \frac{x h_n^{(2)}(x)}{\left[x h_n^{(2)}(x)\right]'} \,, \tag{7.192}$$

$$U_n^l = \frac{\left[k_{l+1}a_{l+1} j_n(k_{l+1}a_{l+1})\right]'}{\left[k_{l+1}a_l j_n(k_{l+1}a_l)\right]'} \frac{\left[k_{l+1}a_l h_n^{(2)}(k_{l+1}a_l)\right]'}{\left[k_{l+1}a_{l+1} h_n^{(2)}(k_{l+1}a_{l+1})\right]'} \,, \tag{7.193}$$

$$V_n^l = \frac{\left[k_{l+1}a_{l+1} j_n(k_{l+1}a_{l+1})\right]}{\left[k_{l+1}a_l j_n(k_{l+1}a_l)\right]} \frac{\left[k_{l+1}a_l h_n^{(2)}(k_{l+1}a_l)\right]}{\left[k_{l+1}a_{l+1} h_n^{(2)}(k_{l+1}a_{l+1})\right]} \,, \tag{7.194}$$

$$Z_n^M = \eta_{M+1} P_n(k_{M+1}a_M) \,, \tag{7.195}$$

and

$$Y_n^M = \frac{1}{\eta_{M+1}} P_n(k_{M+1}a_M) \,. \tag{7.196}$$

At the interface at radius a_l, the impedance and admittance are

$$\begin{aligned} Z_n^{(l)} =& \eta_{l+1} P_n(k_{l+1}a_l) \left[1 - V_n^{(l)} \frac{1 - Z_n^{(l+1)}/\left[\eta_{l+1} P_n(k_{l+1}a_{l+1})\right]}{1 - Z_n^{(l+1)}/\left[\eta_{l+1} Q_n(k_{l+1}a_{l+1})\right]}\right] \cdot \\ & \left[1 - U_n^{(l)} \frac{1 - \eta_{l+1} P_n(k_{l+1}a_{l+1})/Z_n^{(l+1)}}{1 - \eta_{l+1} Q_n(k_{l+1}a_{l+1})/Z_n^{(l+1)}}\right]^{-1} \end{aligned} \tag{7.197}$$

and

$$\begin{aligned} Y_n^{(l)} =& \frac{P_n(k_{l+1}a_l)}{\eta_{l+1}} \left[1 - V_n^{(l)} \frac{1 - \eta_{l+1} Y_n^{(l+1)}/P_n(k_{l+1}a_{l+1})}{1 - \eta_{l+1} Y_n^{(l+1)}/Q_n(k_{l+1}a_{l+1})}\right] \cdot \\ & \left[1 - U_n^{(l)} \frac{1 - P_n(k_{l+1}a_{l+1})/\left[\eta_{l+1} Y_n^{(l+1)}\right]}{1 - Q_n(k_{l+1}a_{l+1})/\left[\eta_{l+1} Y_n^{(l+1)}\right]}\right]^{-1} , \end{aligned} \tag{7.198}$$

where l begins at $M-1$ and ends at $l = 0$. Note that if the core of the sphere is conducting, $Z_n^M \to 0$ and $Y_n^M \to \infty$, thus

$$Z_n^{(M-1)} = \eta_M P_n(k_M a_{M-1}) \frac{1 - V_n^{(M-1)}}{1 - U_n^{(M-1)} P_n(k_M a_M)/Q_n(k_M a_M)} \tag{7.199}$$

and

$$Y_n^{(M-1)} = \frac{P_n(k_M a_{M-1})}{\eta_M} \frac{1 - V_n^{(M-1)} Q_n(k_M a_M)/P_n(k_M a_M)}{1 - U_n^{(M-1)}} \,. \tag{7.200}$$

We use these expressions to compute the field scattered by dielectric and coated conducting spheres in the following sections.

7.9.1.3 Dielectric Sphere

A dielectric sphere comprises a single bounding curve on the interface S_{01} between the free space region R_0 and the interior dielectric region R_1. Applying the PMCHWT formulation on S_{01} yields a linear system of the form

$$\begin{bmatrix} Z^{EJ} & Z^{EM} \\ Z^{HJ} & Z^{HM} \end{bmatrix} \begin{bmatrix} I^J \\ I^M \end{bmatrix} = \begin{bmatrix} V^E \\ V^H \end{bmatrix}, \tag{7.201}$$

where the sub-matrix blocks are

$$Z^{EJ} = \mathrm{L}\big(\mathbf{f}_{S_{01}}, \mathbf{f}_{S_{01}}, R_0\big) + \mathrm{L}\big(\mathbf{f}_{S_{10}}, \mathbf{f}_{S_{10}}, R_1\big) , \tag{7.202}$$

$$Z^{EM} = \mathrm{K}\big(\mathbf{f}_{S_{01}}, \mathbf{g}_{S_{01}}, R_0\big) + \mathrm{K}\big(\mathbf{f}_{S_{10}}, \mathbf{g}_{S_{10}}, R_1\big) , \tag{7.203}$$

$$Z^{HJ} = -\mathrm{K}\big(\mathbf{g}_{S_{01}}, \mathbf{f}_{S_{01}}, R_0\big) - \mathrm{K}\big(\mathbf{g}_{S_{10}}, \mathbf{f}_{S_{10}}, R_1\big) , \tag{7.204}$$

$$Z^{HM} = \frac{\epsilon_0}{\mu_0}\mathrm{L}\big(\mathbf{g}_{S_{01}}, \mathbf{g}_{S_{01}}, R_0\big) + \frac{\epsilon_1}{\mu_1}\mathrm{L}\big(\mathbf{g}_{S_{10}}, \mathbf{g}_{S_{10}}, R_1\big) . \tag{7.205}$$

Each block is understood to contain the $\hat{\mathbf{t}}$ and $\hat{\phi}$ components of all basis and testing functions. The right-hand side vectors are

$$V^E = V^E\big(\mathbf{f}_{S_{01}}, R_0\big) \tag{7.206}$$

and

$$V^H = V^H\big(\mathbf{g}_{S_{01}}, R_0\big) , \tag{7.207}$$

and the solution vectors are

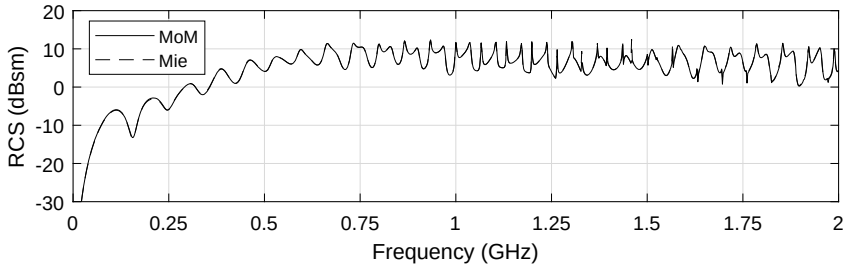
$$I^J = I^J_{S_{01}} \tag{7.208}$$

and

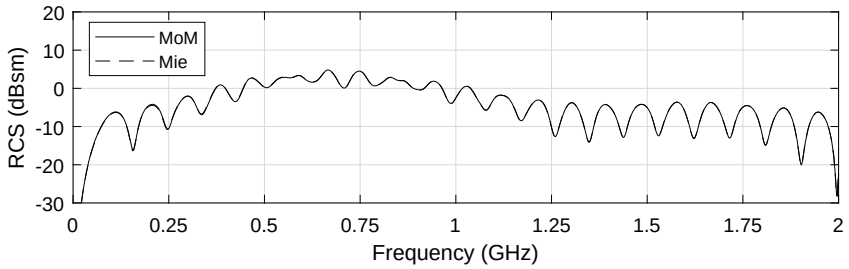
$$I^M = I^M_{S_{01}} . \tag{7.209}$$

7.9.1.3.1 RCS versus Frequency

We first consider the RCS of a dielectric sphere of radius 0.5 meters for frequencies between 10 MHz and 2 GHz. For the Mie terms (7.170) and (7.171), we truncate the summation after 40 modes, and the BoR bounding curve comprises 180 segments of equal length. In Figure 7.8a we compare the Mie series to the MoM for a lossless sphere ($\epsilon_r = 2.56$) in backscattering ($\theta^i = \theta^s = 0$). The agreement is very good. A similar comparison is made in Figure 7.8b for a lossy sphere ($\epsilon_r = 2.56 - j0.102$), where the agreement is again very good. The forward scattering ($\theta^i = 0, \theta^s = \pi$) for each case is summarized in Figures 7.9a and 7.9b, respectively, where the agreement is again quite good.

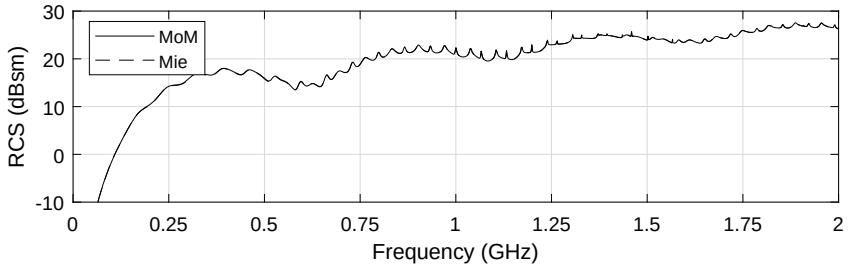


(a) Lossless Sphere ($\epsilon_r = 2.56$)

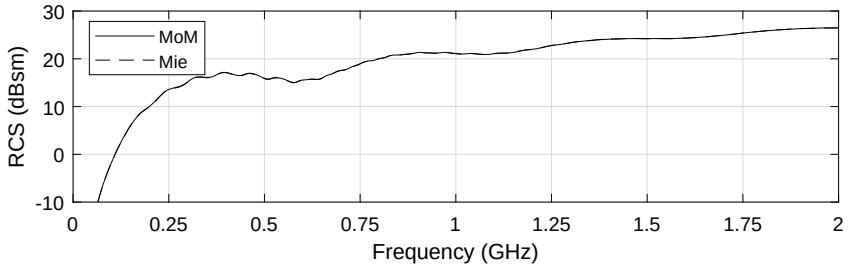


(b) Lossy Sphere ($\epsilon_r = 2.56 - j0.102$)

Figure 7.8: Dielectric Sphere: Backscatter RCS versus Frequency



(a) Lossless Sphere ($\epsilon_r = 2.56$)

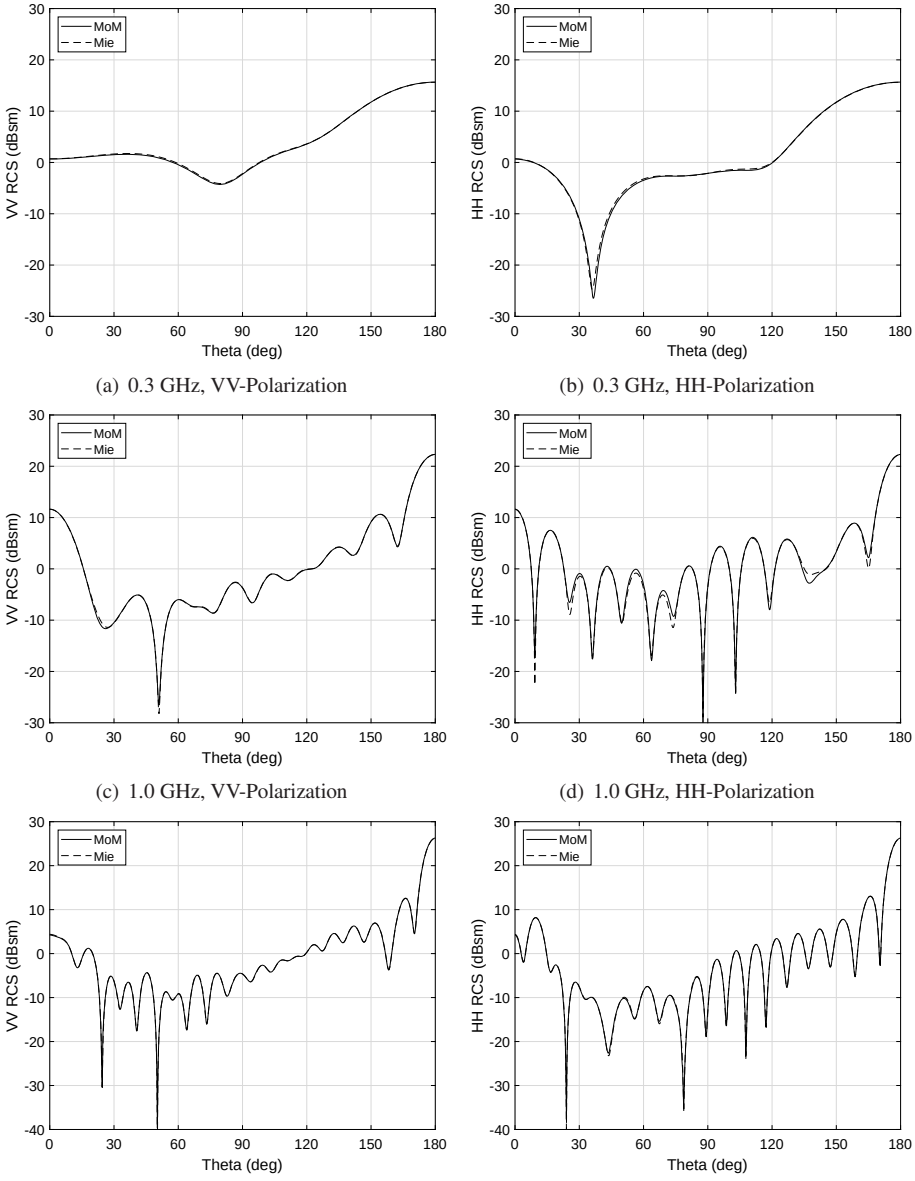


(b) Lossy Sphere ($\epsilon_r = 2.56 - j0.102$)

Figure 7.9: Dielectric Sphere: Forward Scatter RCS versus Frequency

7.9.1.3.2 Bistatic RCS

Using the same parameters as before, we next consider the bistatic RCS at 0.3, 1.0 and 2.0 GHz, for bistatic angles from 0 to 180 degrees. The MoM results are compared to those of the Mie series for the lossless sphere in Figures 7.10a–7.10f. The agreement is very good. The results for the lossy sphere are compared in Figures 7.11a–7.11f, where the agreement is again very good.



(a) 0.3 GHz, VV-Polarization

(b) 0.3 GHz, HH-Polarization

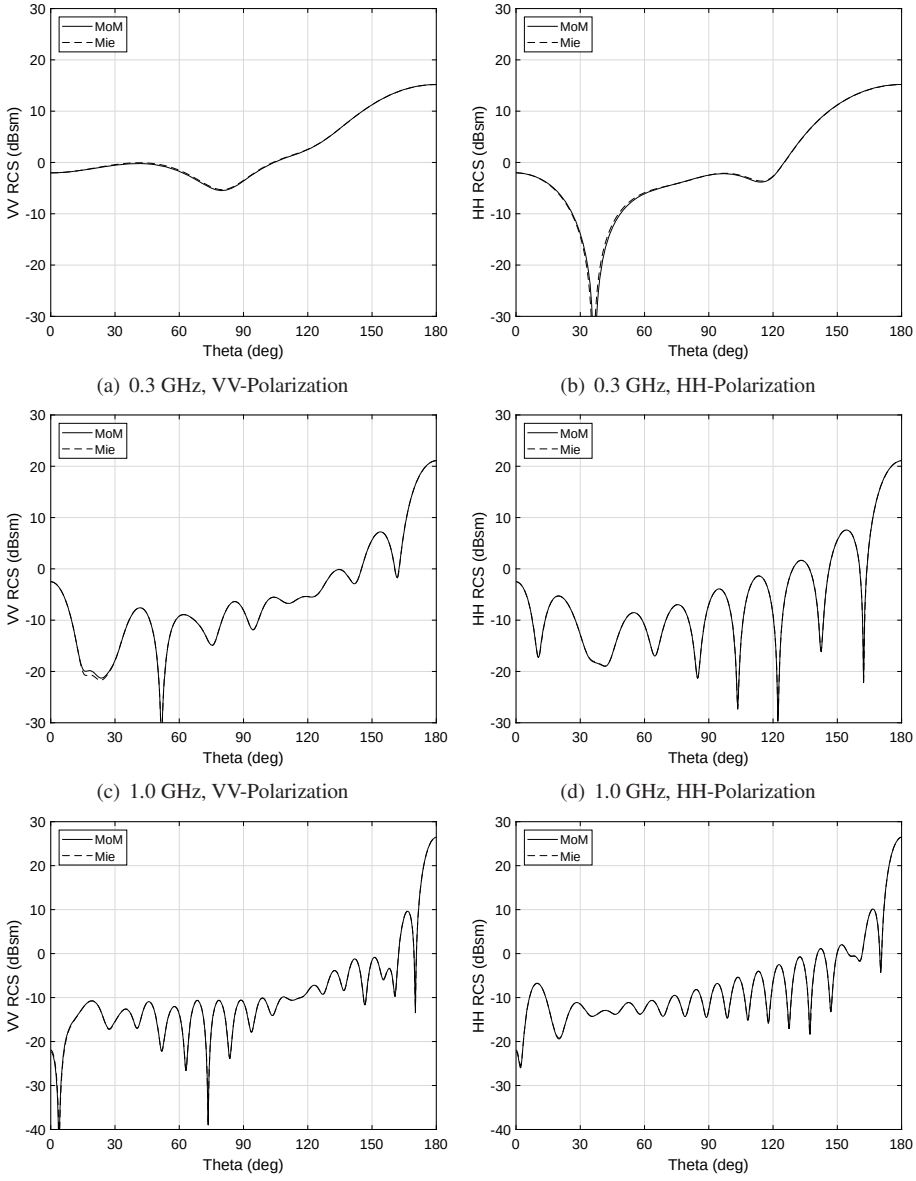
(c) 1.0 GHz, VV-Polarization

(d) 1.0 GHz, HH-Polarization

(e) 2.0 GHz, VV-Polarization

(f) 2.0 GHz, HH-Polarization

Figure 7.10: Lossless Dielectric Sphere ($\epsilon_r = 2.56$): Bistatic RCS



(a) 0.3 GHz, VV-Polarization

(b) 0.3 GHz, HH-Polarization

(c) 1.0 GHz, VV-Polarization

(d) 1.0 GHz, HH-Polarization

(e) 2.0 GHz, VV-Polarization

(f) 2.0 GHz, HH-Polarization

Figure 7.11: Lossy Dielectric Sphere ($\epsilon_r = 2.56 - j0.102$): Bistatic RCS

7.9.1.4 Coated Sphere

A coated conducting sphere comprises two bounding curves: the interface S_{01} between the free space region R_0 and dielectric region R_1, and the interface S_{12} between the dielectric region R_1 and the core conducting region R_2. Applying the PMCHWT and CFIE formulations to this problem yields a linear system of the form

$$\begin{bmatrix} Z^{EJ} + Z^{nHJ} & Z^{EM} + Z^{nHM} \\ Z^{HJ} & Z^{HM} \end{bmatrix} \begin{bmatrix} I^J \\ I^M \end{bmatrix} = \begin{bmatrix} V^E \\ V^H \end{bmatrix}, \tag{7.210}$$

where the sub-matrix blocks are

$$Z^{EJ} = \begin{bmatrix} \mathrm{L}(\mathbf{f}_{S_{01}}, \mathbf{f}_{S_{01}}, R_0) + \mathrm{L}(\mathbf{f}_{S_{10}}, \mathbf{f}_{S_{10}}, R_1) & \mathrm{L}(\mathbf{f}_{S_{10}}, \mathbf{f}_{S_{12}}, R_1) \\ \alpha_c \mathrm{L}(\mathbf{f}_{S_{12}}, \mathbf{f}_{S_{10}}, R_1) & \alpha_c \mathrm{L}(\mathbf{f}_{S_{12}}, \mathbf{f}_{S_{12}}, R_1) \end{bmatrix}, \tag{7.211}$$

$$Z^{nHJ} = \begin{bmatrix} 0 & 0 \\ (1-\alpha_c)\eta_1 \mathrm{nK}(\mathbf{f}_{S_{12}}, \mathbf{f}_{S_{10}}, R_1) & (1-\alpha_c)\eta_1 \mathrm{nK}(\mathbf{f}_{S_{12}}, \mathbf{f}_{S_{12}}, R_1) \end{bmatrix}, \tag{7.212}$$

$$Z^{EM} = \begin{bmatrix} \mathrm{K}(\mathbf{f}_{S_{01}}, \mathbf{g}_{S_{01}}, R_0) + \mathrm{K}(\mathbf{f}_{S_{10}}, \mathbf{g}_{S_{10}}, R_1) \\ \alpha_c \mathrm{K}(\mathbf{f}_{S_{12}}, \mathbf{g}_{S_{10}}, R_1) \end{bmatrix}, \tag{7.213}$$

$$Z^{nHM} = \begin{bmatrix} 0 \\ (1-\alpha_c)\eta_1 \mathrm{nL}(\mathbf{f}_{S_{12}}, \mathbf{g}_{S_{10}}, R_1) \end{bmatrix}, \tag{7.214}$$

$$Z^{HJ} = \left[-\mathrm{K}(\mathbf{g}_{S_{01}}, \mathbf{f}_{S_{01}}, R_0) - \mathrm{K}(\mathbf{g}_{S_{10}}, \mathbf{f}_{S_{10}}, R_1) \mid -\mathrm{K}(\mathbf{g}_{S_{10}}, \mathbf{f}_{S_{12}}, R_1) \right], \tag{7.215}$$

$$Z^{HM} = \left[\tfrac{\epsilon_0}{\mu_0} \mathrm{L}(\mathbf{g}_{S_{01}}, \mathbf{g}_{S_{01}}, R_0) + \tfrac{\epsilon_1}{\mu_1} \mathrm{L}(\mathbf{g}_{S_{10}}, \mathbf{g}_{S_{10}}, R_1) \right], \tag{7.216}$$

where each operator is understood to contain the $\hat{\mathbf{t}}$ and $\hat{\phi}$ components of all basis and testing functions. The right-hand side vectors are

$$V^E = \begin{bmatrix} V^E(\mathbf{f}_{S_{01}}, R_0) \\ 0 \end{bmatrix} \tag{7.217}$$

and

$$V^H = \begin{bmatrix} V^H(\mathbf{g}_{S_{01}}, R_0) \\ 0 \end{bmatrix}, \tag{7.218}$$

and the solution vectors are

$$I^J = \begin{bmatrix} I^J_{S_{01}} \\ I^J_{S_{12}} \end{bmatrix} \tag{7.219}$$

and

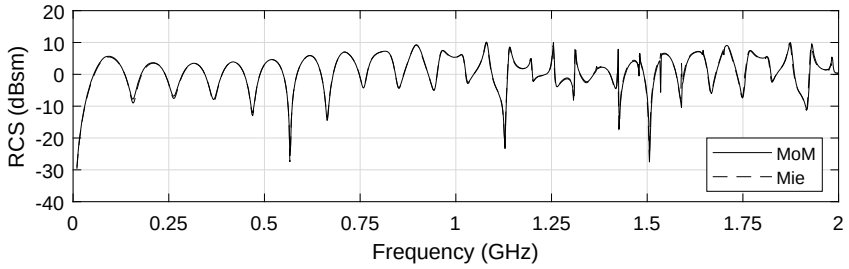
$$I^M = \begin{bmatrix} I^M_{S_{01}} \\ 0 \end{bmatrix}. \tag{7.220}$$

7.9.1.4.1 RCS versus Frequency

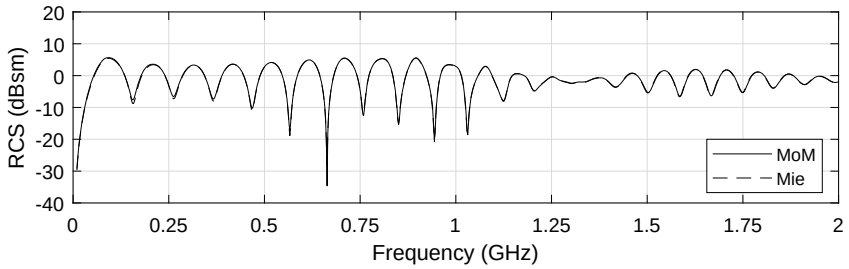
We now consider the RCS of a conducting sphere with dielectric coating for frequencies between 10 MHz and 2 GHz. The conducting core of the sphere has a radius of 0.5 meters, and the dielectric coating has a thickness of 5 centimeters, yielding an outermost radius of 0.55 meters. The bounding curve of the dielectric interface is divided into 180 segments, and the bounding curve of the PEC core is divided into 360 segments. The extra density on the innermost interface is chosen due to the shorter wavelength inside the dielectric coating. The remainder of the run parameters remain the same as before. In Figure 7.12a we compare the Mie series to the MoM in backscattering for a lossless coating ($\epsilon_r = 2.56$). The agreement is very good. In Figure 7.12b is a similar comparison for a lossy coating ($\epsilon_r = 2.56 - j0.102$). The forward-scattering results for each case are compared in 7.13a and 7.13b, respectively, where the agreement is again quite good.

7.9.1.4.2 Bistatic RCS

Using the same parameters as before, we next consider the bistatic RCS at 0.3, 1.0, and 2.0 GHz, for bistatic angles from 0 to 180 degrees. The MoM results are compared with those of the Mie series for the lossless coating in Figures 7.14a–7.14f. The agreement is very good. The results for the lossy coating are compared in Figures 7.15a–7.15f, where the agreement is again very good.

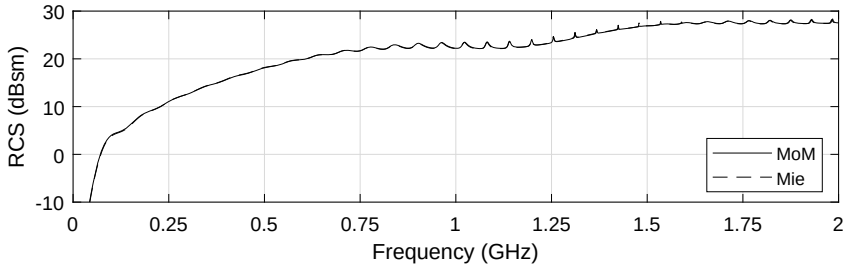


(a) Lossless Coating ($\epsilon_r = 2.56$)

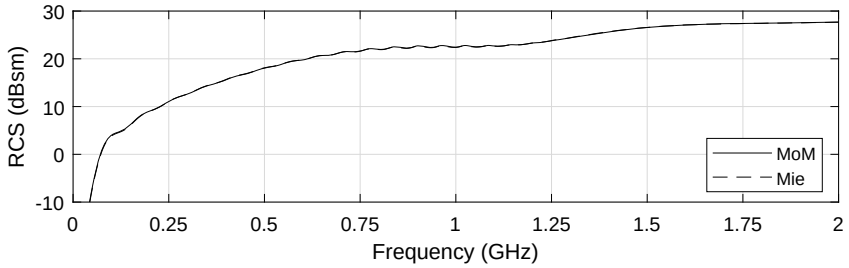


(b) Lossy Coating ($\epsilon_r = 2.56 - j0.102$)

Figure 7.12: Coated Sphere: Backscatter RCS versus Frequency

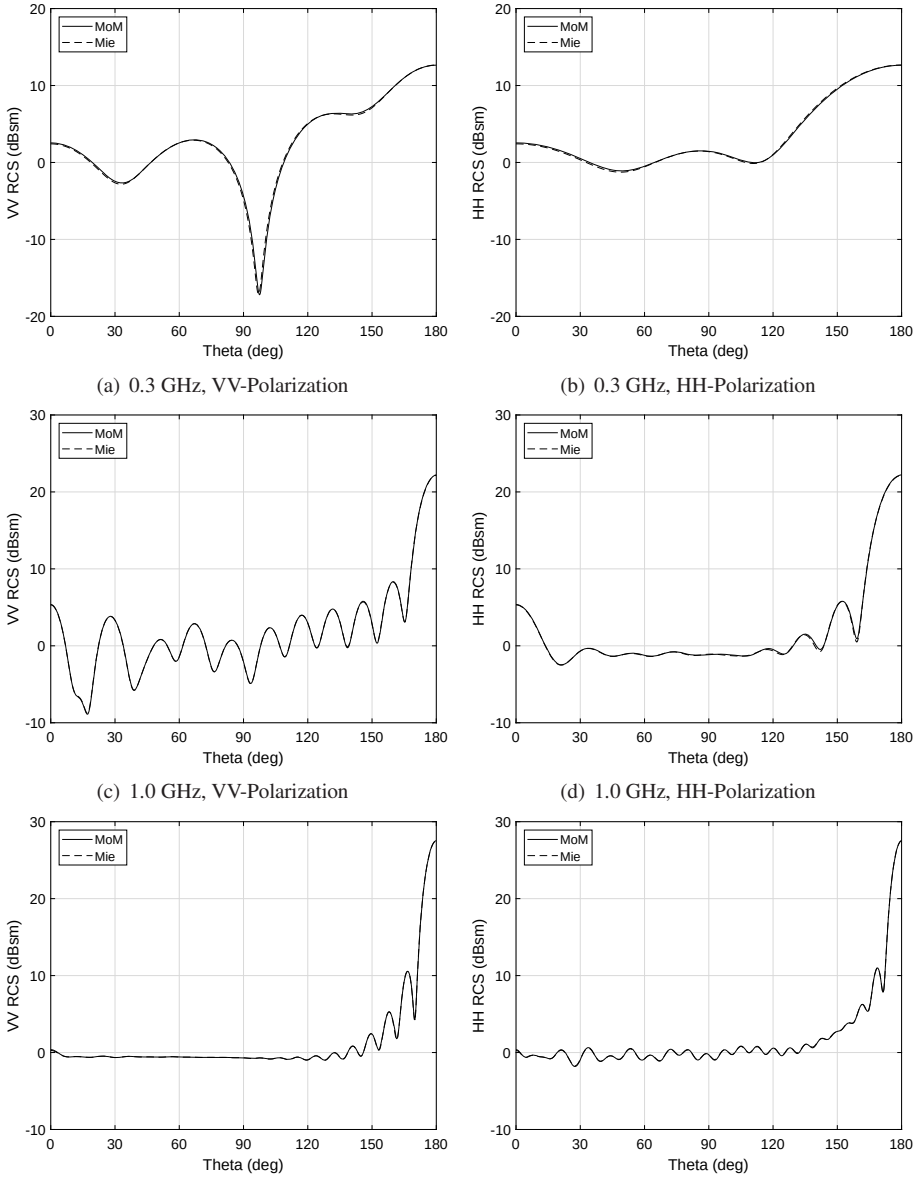


(a) Lossless Coating ($\epsilon_r = 2.56$)



(b) Lossy Coating ($\epsilon_r = 2.56 - j0.102$)

Figure 7.13: Coated Sphere: Forward Scatter RCS versus Frequency



(a) 0.3 GHz, VV-Polarization

(b) 0.3 GHz, HH-Polarization

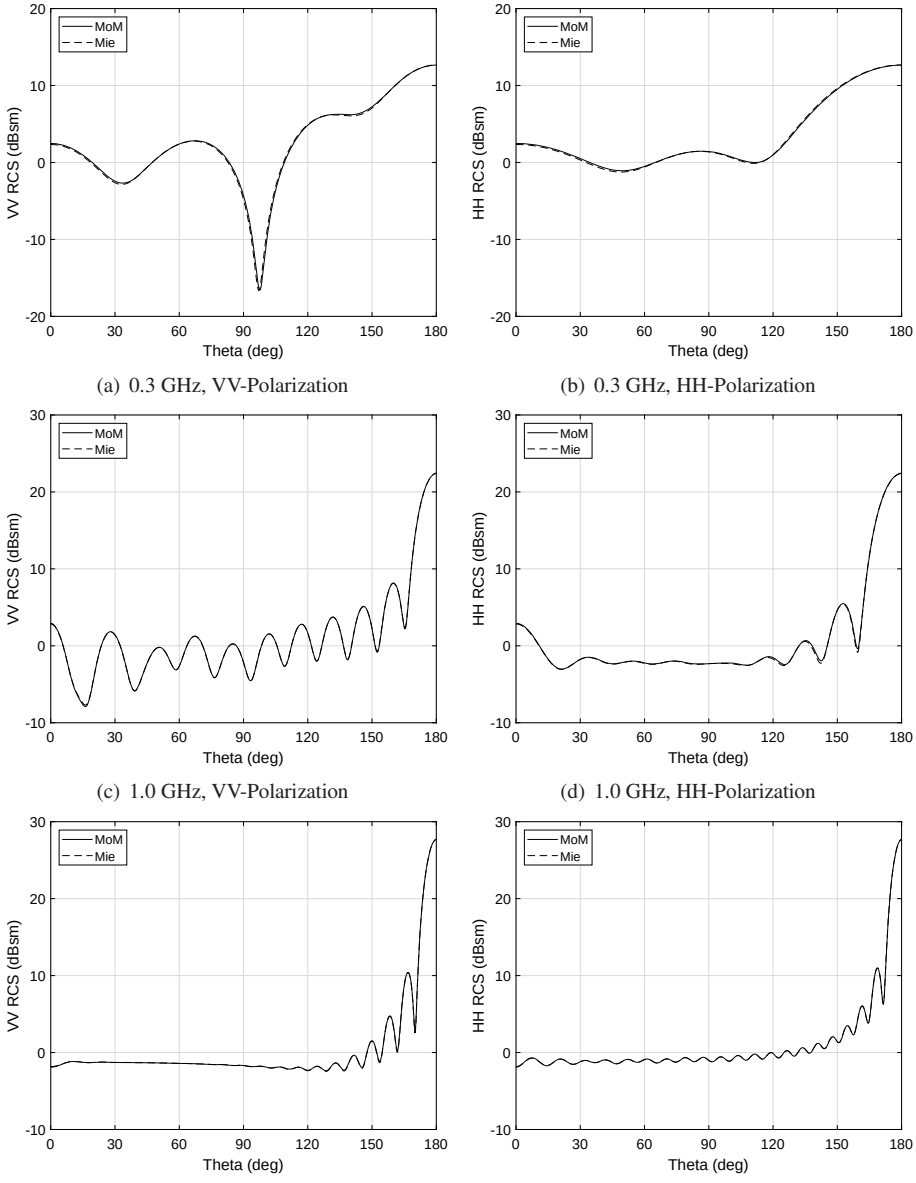
(c) 1.0 GHz, VV-Polarization

(d) 1.0 GHz, HH-Polarization

(e) 2.0 GHz, VV-Polarization

(f) 2.0 GHz, HH-Polarization

Figure 7.14: Lossless Coated Sphere ($\epsilon_r = 2.56$): Bistatic RCS



(a) 0.3 GHz, VV-Polarization

(b) 0.3 GHz, HH-Polarization

(c) 1.0 GHz, VV-Polarization

(d) 1.0 GHz, HH-Polarization

(e) 2.0 GHz, VV-Polarization

(f) 2.0 GHz, HH-Polarization

Figure 7.15: Lossy Coated Sphere ($\epsilon_r = 2.56 - j0.102$): Bistatic RCS

7.9.2 EMCC Benchmark Targets

We will next use the MoM/BoR approach to compute the RCS of several benchmark radar targets described and measured by the EMCC in [9]. The objects considered are the ogive, double ogive, cone-sphere, and cone-sphere with gap. The first three targets are illustrated in Figures 7.16a–7.16c. The test articles used for the measurements were fabricated from aluminum using a numerically controlled mill. In the measurement range, the objects were positioned on a rotating platform in the xy plane. Therefore, computed $\hat{\boldsymbol{\theta}}$-polarization is mapped to measured horizontal polarization, and computed $\hat{\boldsymbol{\phi}}$-polarization is mapped to measured vertical polarization. The comparisons are made using the measurements at 9.0 GHz, and in the plots that follow, measurement data have been shifted slightly in angle to better align them with the computed results.

7.9.2.1 EMCC Ogive

The 10-inch EMCC ogive of Figure 7.16a can be expressed for $0 \leq \phi \leq 2\pi$ as

$$f(x) = \sqrt{1 - \left(\frac{x}{5}\right)^2 \sin^2(22.62^\circ)} - \cos(22.62^\circ) \,, \tag{7.221}$$

$$y(x) = \frac{f(x)\cos\phi}{1 - \cos(22.62^\circ)} \,, \tag{7.222}$$

$$z(x) = \frac{f(x)\sin\phi}{1 - \cos(22.62^\circ)} \,, \tag{7.223}$$

for $-5 \leq x \leq 5$ inches. The BoR bounding curve has 64 segments of equal length, and the MoM calculation is halted after 30 modes. The numerical results are compared with the EMCC measurements in Figures 7.17a and 7.17b for vertical and horizontal polarizations, respectively. The agreement is excellent, including near-tip angles where the cross section is very low.

7.9.2.2 EMCC Double Ogive

The 7.5-inch EMCC double ogive of Figure 7.16b can be expressed for $0 \leq \phi \leq 2\pi$ as

$$g(x) = \sqrt{1 - \left(\frac{x}{2.5}\right)^2 \sin^2(46.6^\circ)} - \cos(46.6^\circ) \,, \tag{7.224}$$

$$y(x) = \frac{g(x)\cos\phi}{1 - \cos(46.4^\circ)} \,, \tag{7.225}$$

$$z(x) = \frac{g(x)\sin\phi}{1 - \cos(46.4^\circ)} \,, \tag{7.226}$$

for $-2.5 \leq x \leq 0$ inches, and

$$f(x) = \sqrt{1 - \left(\frac{x}{5}\right)^2 \sin^2(22.62^\circ)} - \cos(22.62^\circ) \,, \tag{7.227}$$

$$y(x) = \frac{f(x)\cos\phi}{1-\cos(22.62^\circ)}\,, \tag{7.228}$$

$$z(x) = \frac{f(x)\sin\phi}{1-\cos(22.62^\circ)}\,, \tag{7.229}$$

for $0 \leq x \leq 5$ inches. The BoR bounding curve has 64 segments of equal length, and the MoM calculation is halted after 30 modes. The numerical results are compared with the EMCC measurements in Figures 7.18a and 7.18b for vertical and horizontal polarizations, respectively. The agreement is again excellent.

7.9.2.3 EMCC Cone-Sphere

The 27-inch EMCC cone-sphere of Figure 7.16c can be expressed for $0 \leq \phi \leq 2\pi$ as

$$y(x) = 0.87145(x+23.821)\cos\phi\,, \tag{7.230}$$

$$z(x) = 0.87145(x+23.821)\sin\phi\,, \tag{7.231}$$

for $-23.821 \leq x \leq 0$ inches, and

$$y(x) = 2.947\sqrt{1-\left(\frac{x-0.359}{2.947}\right)^2}\cos\phi\,, \tag{7.232}$$

$$z(x) = 2.947\sqrt{1-\left(\frac{x-0.359}{2.947}\right)^2}\sin\phi\,, \tag{7.233}$$

for $0 \leq x \leq 3.306$ inches. The BoR bounding curve has 225 segments of equal length, and the MoM calculation is halted after 30 modes. The numerical results are compared with the EMCC measurements in Figures 7.19a and 7.19b for vertical and horizontal polarizations, respectively. The computed and measured results agree reasonably well at all angles. The side specular in the measured data near 100 degrees is noticeably broader and of lesser amplitude than in the computed data. The reason for this difference is not known, and was not mentioned in [9].

7.9.2.4 EMCC Cone-Sphere with Gap

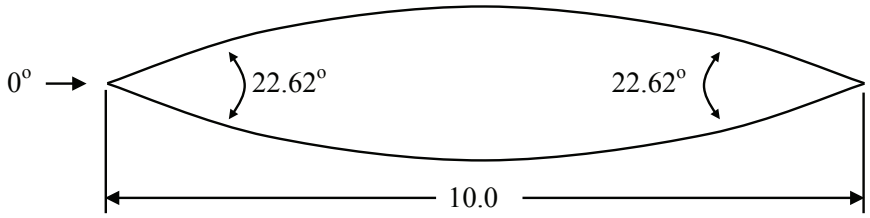
The EMCC cone-sphere with gap is identical to the cone-sphere except that a square groove of depth $\frac{1}{4}$ inch is cut into the target near the cone-sphere junction point. The gap can be expressed for $0 \leq \phi \leq 2\pi$ as

$$y(x) = 2.697\cos\phi\,, \tag{7.234}$$

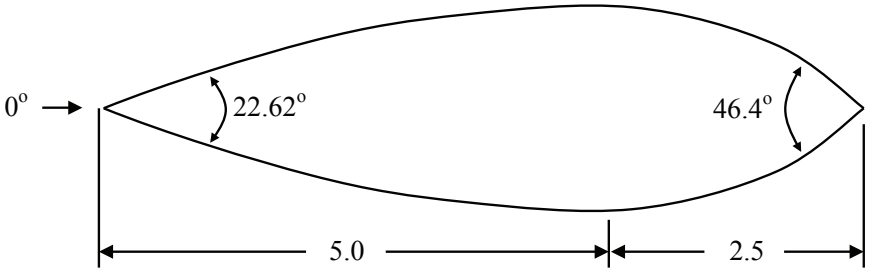
and

$$z(x) = 2.697\sin\phi\,, \tag{7.235}$$

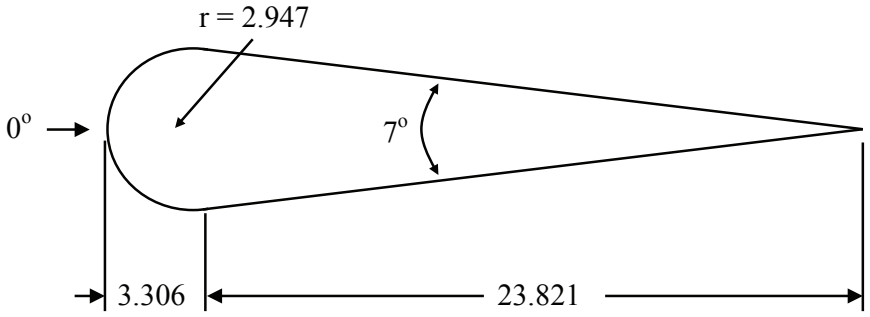
for $0 \leq x \leq 0.25$ inches. At 9.0 GHz, the dimensions of the gap are approximately $\lambda/5$. To generate the bounding curve, an additional 25 segments were added to the cone-sphere model in the vicinity of the gap, yielding a total of 250 boundary segments.



(a) Ogive



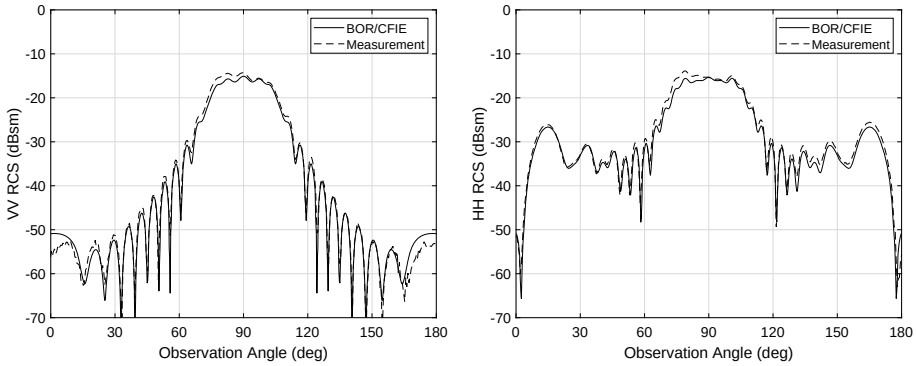
(b) Double Ogive



(c) Cone-Sphere

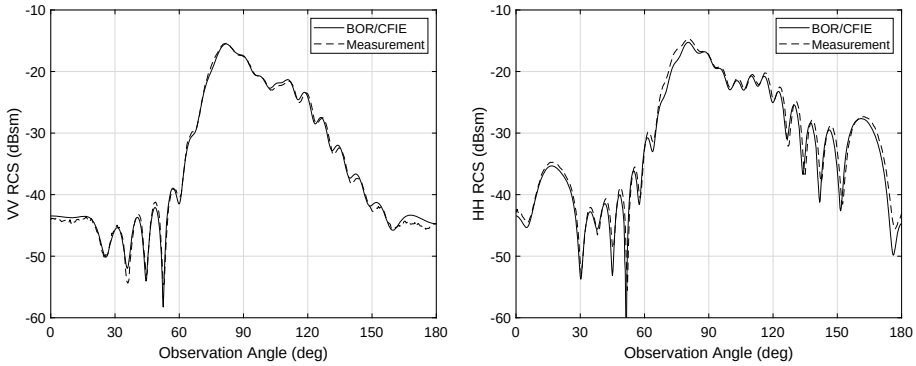
Figure 7.16: EMCC BoR Targets (Dimensions in Inches)

The numerical results are compared with the EMCC measurements in Figures 7.20a and 7.20b for vertical and horizontal polarizations, respectively. The agreement is again excellent. The presence of the gap has a significant effect on the backscattered field, especially in horizontal polarization.



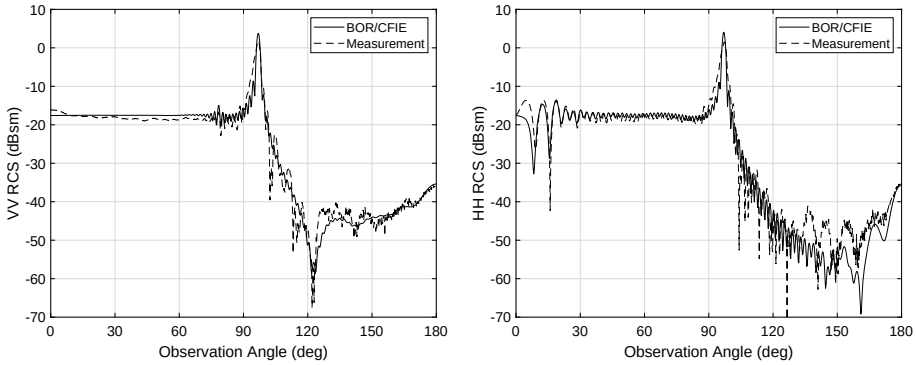
(a) Vertical Polarization (b) Horizontal Polarization

Figure 7.17: EMCC Ogive: BoR versus Measurement at 9.0 GHz



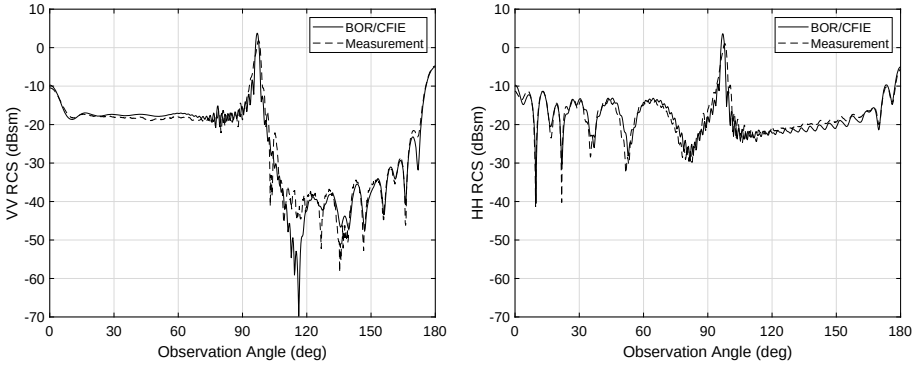
(a) Vertical Polarization (b) Horizontal Polarization

Figure 7.18: EMCC Double Ogive: BoR versus Measurement at 9.0 GHz



(a) Vertical Polarization (b) Horizontal Polarization

Figure 7.19: EMCC Cone-Sphere: BoR versus Measurement at 9.0 GHz



(a) Vertical Polarization (b) Horizontal Polarization

Figure 7.20: EMCC Cone-Sphere with Gap: BoR versus Measurement at 9.0 GHz

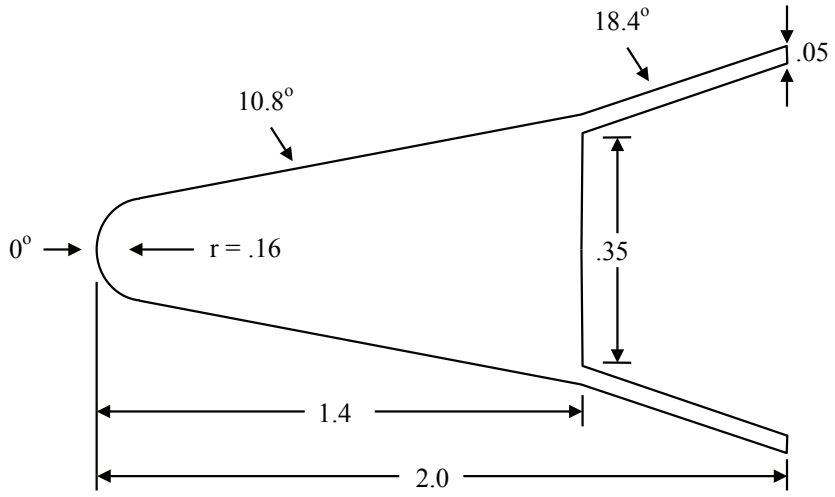
7.9.3 Biconic Reentry Vehicle

We next consider a biconic reentry vehicle (RV) whose dimensions are outlined in Figure 7.21a. The RV has a large nose and deeply recessed rear cavity that should be significant sources of backscatter. The three-dimensional shape of the RV is illustrated at forward and rear aspects in Figures 7.21b and 7.21c, respectively. The total length of the BoR bounding curve for this object is approximately 3.2 meters.

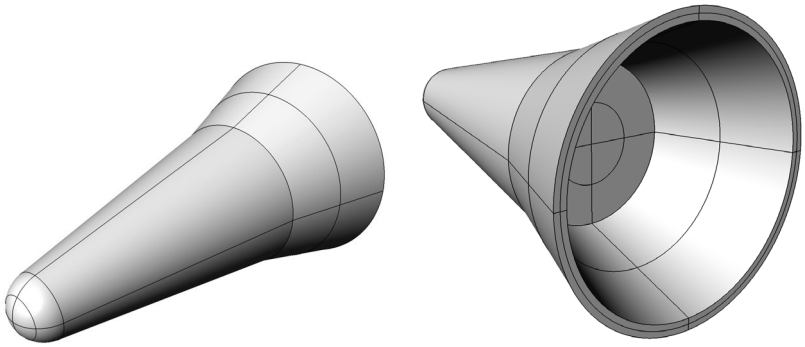
When studying the backscattering behavior of a target, it is very often useful to consider its range profile over a wide range of monostatic angles. This allows for isolation of the target's scattering features, often referred to as *scattering centers*. Therefore, we will compute the complex-valued scattered far field of the RV for frequencies ranging from 5 to 6 GHz (C-Band), for monostatic angles from 0 to 180 degrees. At 6 GHz, the length of the bounding curve of the RV is approximately 64 wavelengths. Our numerical model uses 577 boundary segments, which is approximately 10 segments per wavelength.

For visualization purposes, we compute the range profiles across all incident angles and stack them together to create a two-dimensional figure called a *range-aspect-intensity* (RAI) plot. RAI plots for vertical and horizontal polarizations are shown in Figures 7.22a and 7.22b, respectively. The choice of bandwidth results in a down-range resolution of approximately 15 centimeters, and a Hamming window is used to reduce range sidelobes. Clearly visible at forward-scattering angles are the large scattering responses from the nose and the rear base edge. At rear aspects, the multiple bounce returns from inside the cavity clearly dominate the response, giving rise to significant returns from down-range locations.

We can further isolate the scattering centers of the target by generating a two-dimensional *range-Doppler* image. Such an image is generated by computing the FFT of each range line over a small range of angles. If we assume that the Doppler frequency of each bin remains constant across the integration interval, then we can achieve



(a) Biconic Reentry Vehicle Dimensions



(b) Three-Dimensional View (c) Three-Dimensional View

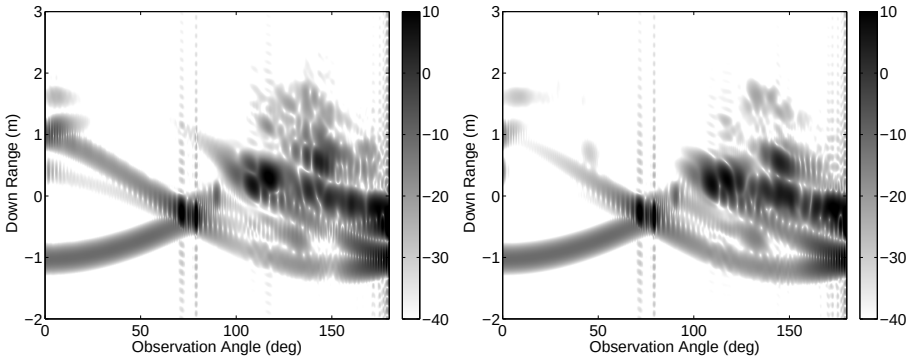
Figure 7.21: Biconic Reentry Vehicle

a cross-range resolution given by [10]

$$\Delta_{cr} = \frac{\lambda_0}{2\Delta_\theta} \,, \tag{7.236}$$

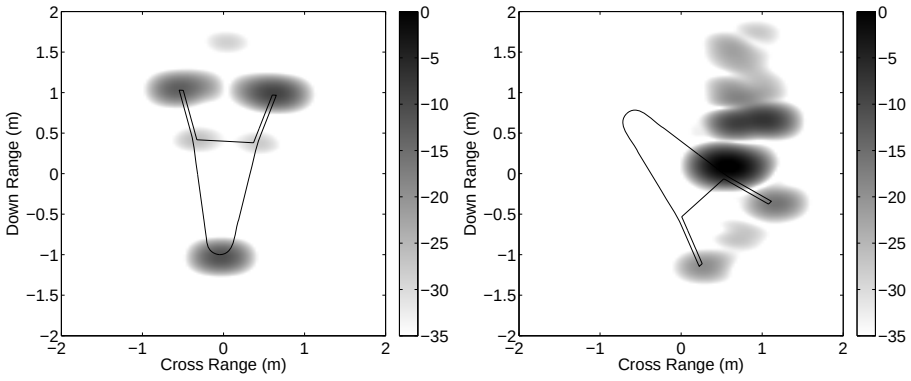
where λ_0 is the average wavelength, and Δ_θ is the angular extent of the integration. For an extent of about 6 degrees, the cross-range resolution is approximately 0.26 meters at 5.5 GHz. Range-Doppler images centered at observation angles of 3 and 138 degrees are shown in Figures 7.23a and 7.23b, respectively, for vertical polarization. A Hamming window is used in the cross-range dimension to reduce sidelobes. Superimposed onto each image is the two-dimensional outline of the RV, allowing us to register the scattering features. At the forward aspect, the scattering centers at the nose and stationary phase points of the base edge (sometimes referred to as slipping scatterers) are clearly visible. The joint between the two frustums is also visible, as well as the

faint double-diffraction response located slightly past the target. At the rear aspect, the delayed returns dominate the image. These scattering centers appear to originate from off-body locations, obscuring the true shape of the target. Such features are often detrimental to automated target recognition (ATR) algorithms that use the object's shape as a discrimination feature. Real-world reentry vehicles often have hoses, propellant tanks, wiring, and assorted electronics in the rear cavity that give rise to additional multiple-bounce behavior. As a result, radar observations of such a target could result in an apparent length several times that of the true object.



(a) VV-Polarization (b) HH-Polarization

Figure 7.22: Biconic Reentry Vehicle: C-Band Range Profiles (dBsm)



(a) Center Angle = 3 Degrees (b) Center Angle = 138 Degrees

Figure 7.23: Biconic Reentry Vehicle: C-Band Range-Doppler Images (dBsm)

7.10 Treatment of Junctions

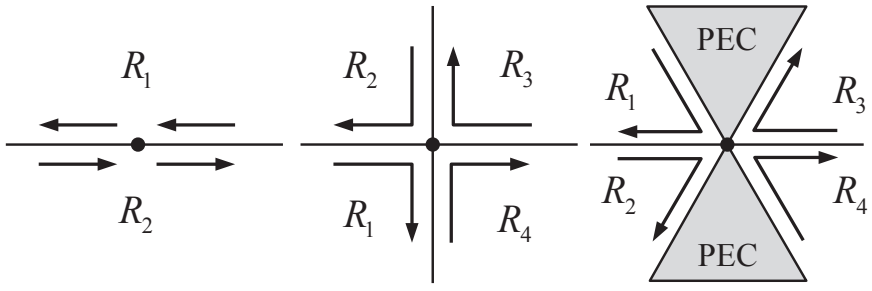
Thus far, our treatment has only considered interfaces between two regions. Points at which three or more regions meet are called *junctions*, and at these, the boundary conditions and orientation of vector basis functions must be considered more carefully. In this section, we will consider the treatment, placement, and orientation of the longitudinal and azimuthal vectors at several types of junctions in BoR problems. We also refer the reader to Section 8.6 for an in-depth discussion of the treatment of the boundary conditions and enforcement of integral equations at junctions of general configuration.

7.10.1 Orientation of Basis Functions

In Section 7.7, we examined the assignment and orientation of basis functions at an interface between two regions. We will now generalize this further by considering junctions between N regions, where one or more of these regions may be conducting. In a BoR geometry, junctions occur where an endpoint is shared by three or more boundary segments.

7.10.1.1 Longitudinal Basis Vectors

According to Section 7.7, the longitudinally oriented basis functions assigned to a point on the interface between two dielectric regions must have opposing directions on each side, as shown in Figure 7.24a. Consider now the interface between three or more dielectric regions, as shown in Figure 7.24b. Because Kirchhoff's current law must be satisfied in each region, the basis vectors must flow past the common point in a clockwise (or counterclockwise) manner, as shown. Furthermore, the boundary conditions stipulate that these basis functions must have the same coefficient. If we now make one or more of the regions conducting, as in Figure 7.24c, this assignment will remain valid for dielectric interfaces that lie between conductors. Thus, the oriented basis functions in R_1 and R_2 will be combined into one unknown, as will the basis functions in R_3 and R_4.

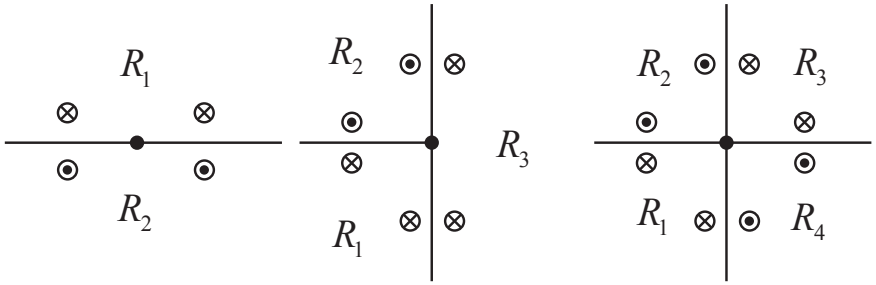


(a) Single Interface (b) Dielectric Junction (c) Conducting Junction

Figure 7.24: Orientation of Longitudinal Basis Vectors

7.10.1.2 Azimuthal Basis Vectors

At the intersection between two regions, as shown in Figure 7.25a, the azimuthally oriented basis functions assigned to the common point have a $+\hat{\phi}$ orientation in R_1, and a $-\hat{\phi}$ orientation in R_2. Under this arrangement, the boundary conditions at the interface are satisfied, and the basis functions on each side of the interface can be combined into a single unknown. If we now increase the number of dielectric regions meeting at this point to any odd number greater than or equal to three, this arrangement is no longer possible. This is illustrated in Figure 7.25b for a junction between three regions, where the boundary condition is not satisfied at the interface between R_1 and R_3. This implies that at the intersection of an odd number of dielectric regions, we must use half-triangles on each segment and assign separate coefficients to each. Increasing the number of regions to four, as in Figure 7.25c, we see that the boundary conditions are again satisfied, and we can again use full triangle functions and combine the unknowns into a single unknown. This approach is similar to that in [4], except that the approach taken there suggests using half-triangles for all azimuthal *and* longitudinal functions at a junction, regardless of the number of regions meeting there.



(a) Two Regions (Good) (b) Three Regions (Not Good) (c) Four Regions (Good)

Figure 7.25: Orientation of Azimuthal Basis Vectors

7.10.2 Examples with Junctions

We now consider several examples involving dielectric and dielectric/conducting objects with junctions.

7.10.2.1 Dielectric Sphere with Septum

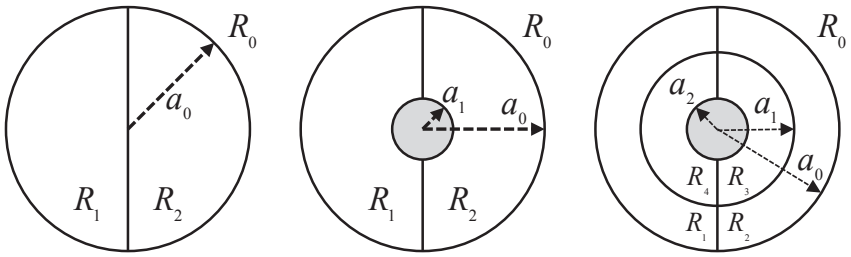
We will first consider the dielectric sphere depicted in Figure 7.26a, where the sphere has been split into two hemispheres of equal size. There are now three dielectric regions: the free space region R_0 and the two dielectric halves R_1 and R_2. This object has a single junction at the intersection of the three regions.

7.10.2.1.1 Results

A good way to test the effectiveness of the junction treatment is to treat R_1 and R_2 as independent regions having identical dielectric properties. This effectively creates a homogeneous dielectric sphere, and the MoM/BoR results can be compared against the Mie series solution. The outermost radius of the sphere is $a_0 = 1\lambda_0$. The dielectric parameter of both regions is $\epsilon_r = 2.56$, and for the Mie solution, $N = 40$. The bounding curves are subdivided into 10 segments per wavelength in each region. The MoM results are compared with the Mie series in Figures 7.27a and 7.27b for vertical and horizontal polarization, respectively, where the comparison is very good.

7.10.2.2 Coated Sphere with Septum

We next consider a conducting sphere with a dielectric coating, depicted in Figure 7.26b. The coating is again separated into two partial hemispheres of equal size. There are three dielectric regions: the free space region R_0, and the two hemispherical dielectric regions R_1 and R_2. The conducting core comprises an additional region, R_3, which is not labeled. This object has two junctions: a junction at the intersection of R_0, R_1, and R_2, and another at the intersection of R_1, R_2, and R_3.



(a) Dielectric Sphere (b) Coated Sphere (c) Stratified Sphere

Figure 7.26: Spheres with a Hemispherical Division

7.10.2.2.1 Results

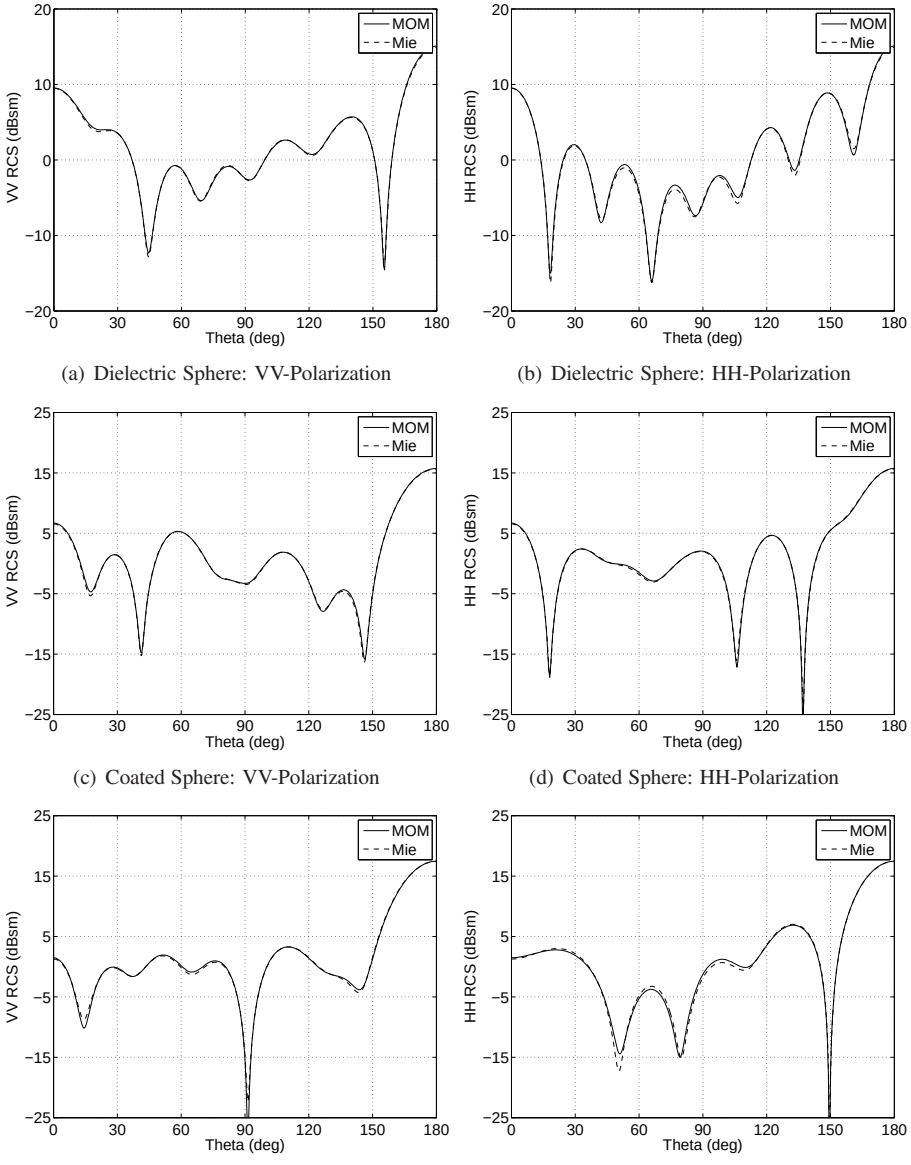
R_1 and R_2 are again treated as independent regions having identical dielectric properties. The radius of the conducting core is $a_1 = 0.25\lambda_0$, and the radius of the coating is $a_0 = 1\lambda_0$. The dielectric parameter of both regions is $\epsilon_r = 5$, and for the Mie solution, $N = 40$. The bounding curves are subdivided into 10 segments per wavelength in each region. The MoM results are compared with the Mie series in Figures 7.27c and 7.27d for vertical and horizontal polarization, respectively, where the agreement is again very good.

7.10.2.3 Stratified Sphere with Septum

We next consider a conducting sphere with a stratified dielectric coating, depicted in Figure 7.26c. The stratified coatings are split into two partial hemispheres of equal size. There are five dielectric regions: the free space region R_0, the hemispherical regions of the outermost coating (R_1 and R_2) and the hemispherical regions of the innermost coating (R_3 and R_4). The conducting core comprises an additional region, R_5, which is not labeled. This object has three junctions: A junction at the intersection of R_0, R_1, and R_2, one at the intersection of R_1, R_2, R_3, and R_4, and another at the intersection of R_3, R_4, and R_5.

7.10.2.3.1 Results

For this example, regions R_1 and R_2 are assigned a dielectric parameter of $\epsilon_r = 5.0$, and regions R_3 and R_4 are assigned $\epsilon_r = 7.0$. The radius of the conducting core is $a_2 = 0.125\lambda_0$, the radius of the innermost coating is $a_1 = 0.6\lambda_0$, and the radius of the outermost coating is $a_0 = 1\lambda_0$. The bounding curves are subdivided into 10 segments per wavelength in each region, and for the Mie solution, $N = 40$. The MoM results are compared with the Mie series in Figures 7.27e and 7.27f for vertical and horizontal polarization, respectively, where the agreement is again very good.



(a) Dielectric Sphere: VV-Polarization

(b) Dielectric Sphere: HH-Polarization

(c) Coated Sphere: VV-Polarization

(d) Coated Sphere: HH-Polarization

(e) Stratified Sphere: VV-Polarization

(f) Stratified Sphere: HH-Polarization

Figure 7.27: Spheres with Junctions: Bistatic RCS

7.10.2.4 Monoconic Reentry Vehicle with Dielectric Nose

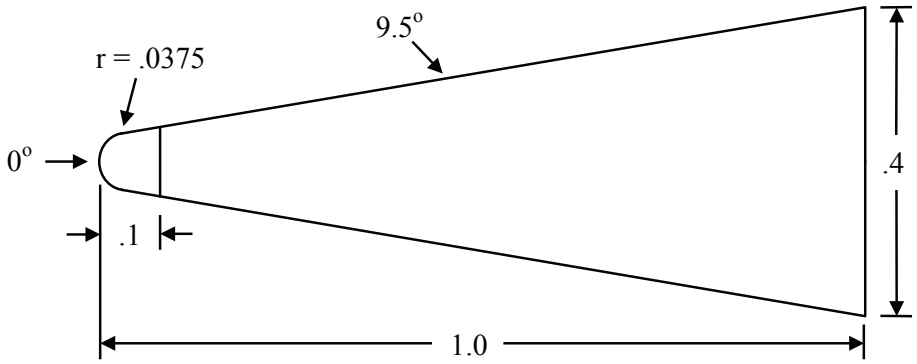
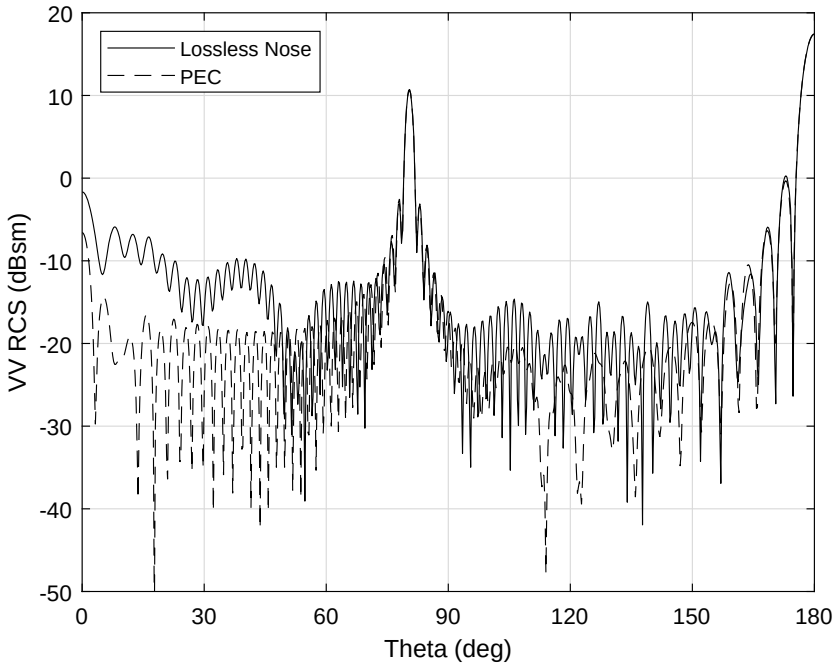


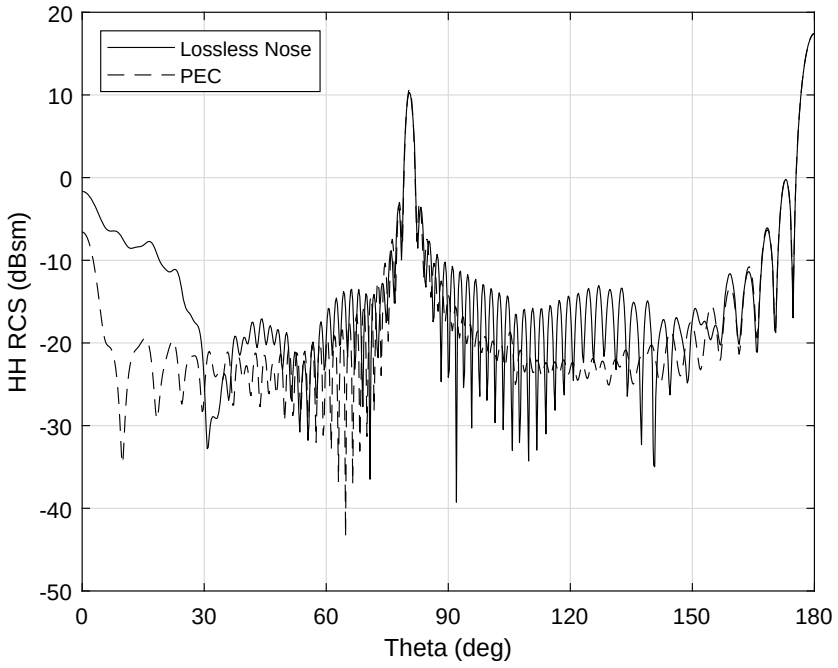
Figure 7.28: Monoconic Reentry Vehicle Dimensions (meters)

Finally, we will examine a monoconic reentry vehicle (RV) whose dimensions are outlined in Figure 7.28. The RV has a length of 1 meter and a base diameter of 0.4 meters, with a cone angle of 9.5 degrees. The dielectric section is 10 centimeters in length, and the nose tip has a radius of curvature of 3.75 centimeters. This problem has three regions: the free space region R_0, the dielectric (nose tip) region R_1, and the conducting (frustum) region R_2. As reentry vehicles typically have nose tips made of an ablative material, this is a somewhat realistic example.

7.10.2.4.1 Results

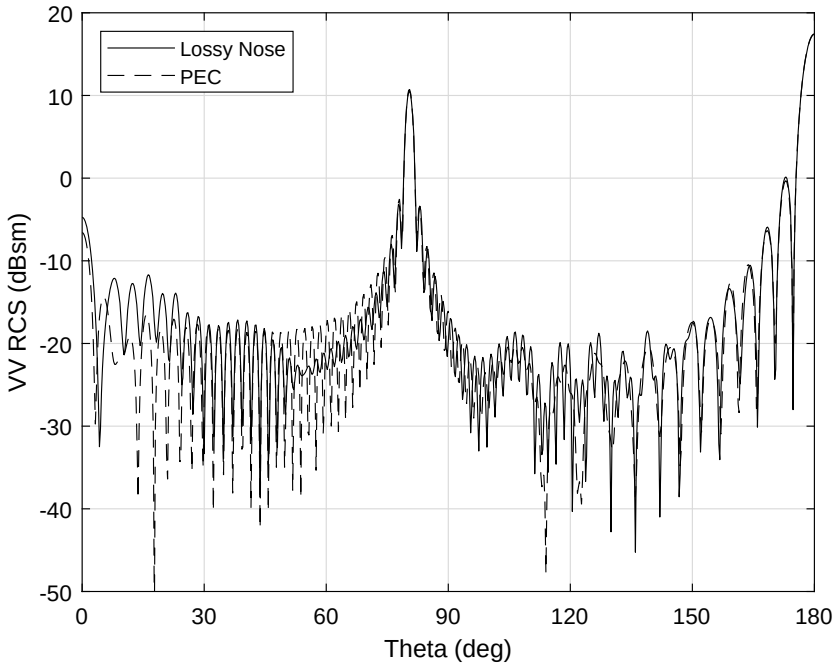
We compute the monostatic RCS of the RV at 5.0 GHz, and consider the nose tip with lossless ($\epsilon_r = 5$) and lossy ($\epsilon_r = 5.0 - j0.25$) dielectric parameters. The interfaces are constructed as follows: 223 segments for conducting frustum (S_{02}), 25 segments for the nose (S_{01}), and 19 segments for the interface (septum) S_{12} between the frustum and nose. The RV with a lossless nose tip is compared to a perfectly conducting RV of the same dimensions in Figures 7.29a and 7.29b for vertical and horizontal polarizations, respectively. The RV with the dielectric nose has a significantly higher RCS at many aspect angles, particularly below 30 degrees. This is due to the many multiple-bounces inside the nose. A similar comparison is done for the RV with lossy nose in Figures 7.30a and 7.30b. The RCS has been significantly reduced from the lossless case, although it is still significantly higher at nose-forward aspect angles, particularly in horizontal polarization.

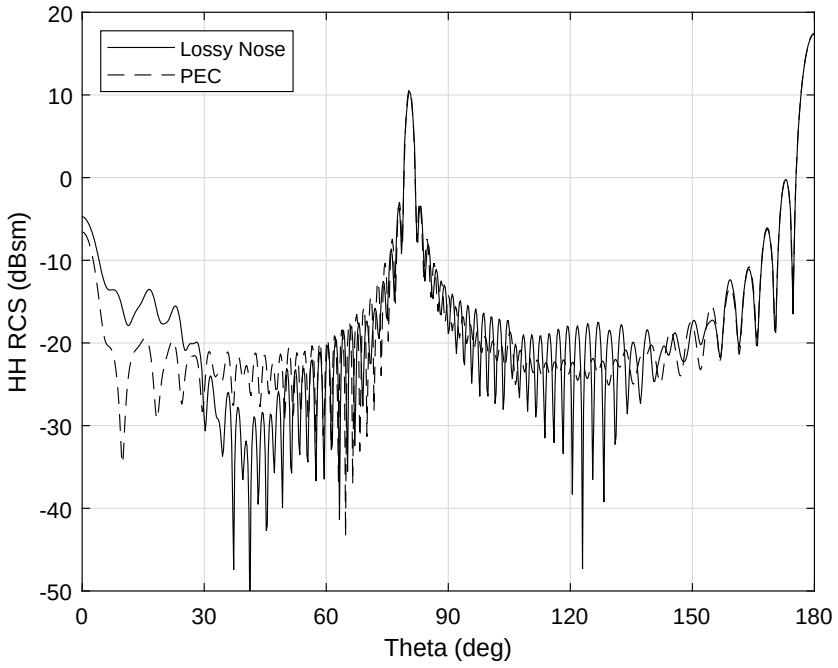




(b) HH-Polarization

Figure 7.29: Monoconic RV RCS: Lossless Nose versus PEC at 5.0 GHz





(b) HH-Polarization

Figure 7.30: Monoconic RV RCS: Lossy Nose versus PEC at 5.0 GHz

References

[1] R. Mautz and R. Harrington, "H-field, E-field and combined solutions for bodies of revolution," Tech. Rep. Report RADC-TR-77-109, Rome Air Development Center, Griffiss AFB, N.Y., March 1977.

[2] L. N. Medgyesi-Mitschang and J. M. Putnam, "Electromagnetic scattering from axially inhomogeneous bodies of revolution," *IEEE Trans. Antennas Propagat.*, vol. 32, pp. 796–806, March 1984.

[3] M. Abramowitz and I. Stegun, *Handbook of Mathematical Functions*. National Bureau of Standards, 1966.

[4] L. N. Medgyesi-Mitschang and J. M. Putnam, "Combined field integral equation formulation for inhomogeneous two- and three-dimensional bodies: The junction problem," *IEEE Trans. Antennas Propagat.*, vol. 39, pp. 667–672, May 1991.

[5] K. Faison, "The Electromagnetics Code Consortium," *IEEE Antennas Propagat. Magazine*, vol. 30, pp. 19–23, February 1990.

[6] G. T. Ruck, ed., *Radar Cross Section Handbook*. Plenum Press, 1970.

[7] B. R. Mahafza, *Introduction to Radar Analysis*. CRC Press, 1998.

[8] A. W. Doerry, "Catalog of window taper functions for sidelobe control," Tech. Rep. SAND2017-4042, Sandia National Laboratories, April 2017.

[9] A. C. Woo, H. T. G. Wang, M. J. Schuh, and M. L. Sanders, "Benchmark radar targets for the validation of computational electromagnetics programs," *IEEE Antennas Propagat. Magazine*, vol. 35, pp. 84–89, February 1993.

[10] A. Ausherman, A. Kozma, J. Waker, H. M. Jones, and E. C. Poggio, "Developments in radar imaging," *IEEE Trans. Aerospace Electron. Syst.*, vol. 20, pp. 363–400, July 1984.